



Review

Mathematical methods for modeling the microcirculation

Julia C. Arciero ¹, Paola Causin ^{2,*} and Francesca Malgaroli ²

¹ Department of Mathematical Sciences, IUPUI, 402 N. Blackford, LD 270, Indianapolis IN 46202, USA

² Department of Mathematics, University of Milan, via Saldini 50, 20133 Milano, Italy

* **Correspondence:** Email: paola.causin@unimi.it; Tel: +390250316170.

Abstract: The microcirculation plays a major role in maintaining homeostasis in the body. Alterations or dysfunctions of the microcirculation can lead to several types of serious diseases. It is not surprising, then, that the microcirculation has been an object of intense theoretical and experimental study over the past few decades. Mathematical approaches offer a valuable method for quantifying the relationships between various mechanical, hemodynamic, and regulatory factors of the microcirculation and the pathophysiology of numerous diseases. This work provides an overview of several mathematical models that describe and investigate the many different aspects of the microcirculation, including geometry of the vascular bed, blood flow in the vascular networks, solute transport and delivery to the surrounding tissue, and vessel wall mechanics under passive and active stimuli. Representing relevant phenomena across multiple spatial scales remains a major challenge in modeling the microcirculation. Nevertheless, the depth and breadth of mathematical modeling with applications in the microcirculation is demonstrated in this work. A special emphasis is placed on models of the retinal circulation, including models that predict the influence of ocular hemodynamic alterations with the progression of ocular diseases such as glaucoma.

Keywords: microcirculation; blood flow; oxygen transport; autoregulation; fluid-structure interaction problems; mathematical model; retinal microcirculation

1. Introduction

The microcirculation is the collective name for the smallest (<150 μm in diameter) blood vessels in the body. As a first approximation, it consists of blood vessels that are too small to be seen

with the naked eye. Microcirculatory vessels are the site of control of tissue perfusion, blood-tissue exchange, and tissue blood volume. Each of these functions can be associated, though not exclusively, with a specific type of microvascular segment: arterioles, capillaries and venules. Arterioles are known as resistance vessels since a major fraction of total blood pressure dissipation occurs across them. Local and extrinsic stimuli (e.g., neural, metabolic, and mechanical) act on the thick muscular wall of arterioles, exerting control over the vessel diameter and modulating the level of local blood flow. The capillaries are the site of major exchange between blood and tissue. Nutrients and other molecules diffuse or are transported across the capillary wall to sustain life of the body's cells. Finally, venules are classified as capacitance vessels because most of the tissue blood volume is localized in these microvessels. Comprehensive, recent reviews on the biological, anatomical and structural aspects of the microcirculation can be found in [1,2,3]. In addition, there exist several review works focused on the microcirculation in specific organs and tissues, see, e.g., [4] for brain, [5] for kidneys, [6] for gastrointestinal organs and [7] for lungs.

Various techniques have been used to obtain a substantial amount of hemodynamic and geometric information about the microcirculation. For example, data has been obtained from studying whole organs both *in vivo* and in perfused conditions. The results of these studies are averaged quantities that give indirect information about microcirculatory behavior. Modern non-invasive imaging techniques are used to obtain data about normal and diseased states in microcirculation. Imaging techniques—including MRI, imaging with light and sound, optical techniques such as laser Doppler and multispectral imaging—show microvascular structure and provide measures of function via perfusion, oxygenation, or permeability parameters. We refer to [8,9,10] for reviews on these imaging techniques.

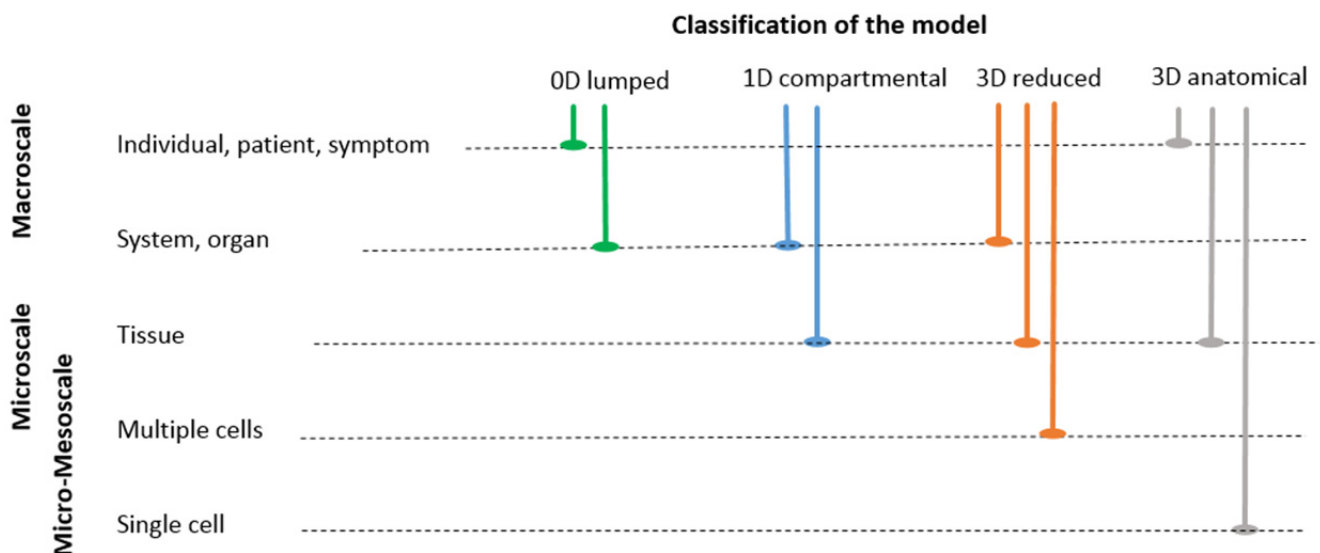


Figure 1. Conceptual illustration of the different scales addressed by mathematical models of the microcirculation.

The role of theoretical models of the microcirculation has been described previously by Secomb in [11]. In this work, Secomb remarks that mathematical modelers of the microcirculation have pioneered the integration of knowledge across multiple levels of biological organization. He

classifies models as phenomenological, qualitative, quantitative, and predictive. In the present review, we will adopt a similar classification for microcirculation models; furthermore, in our model classification we will also highlight the spatial dimension of the models (0D to 3D) and their mathematical features. In Figure 1, we present a schematic illustration of the classification and scale of mathematical models of the microcirculation that are reviewed in this study. Geometrically reduced 0D/1D models are capable of providing very useful information on whole-scale vascular beds or organs (e.g., the brain or kidney), even if they cannot provide a spatially-resolved information. On the other hand, 3D models can capture detailed and patient-specific components of the vascular anatomy, at the price of a rapidly increasing computational cost. The full range of models between 0D and 3D representations offer a balance of information and can be used to study a large spectrum of scales.

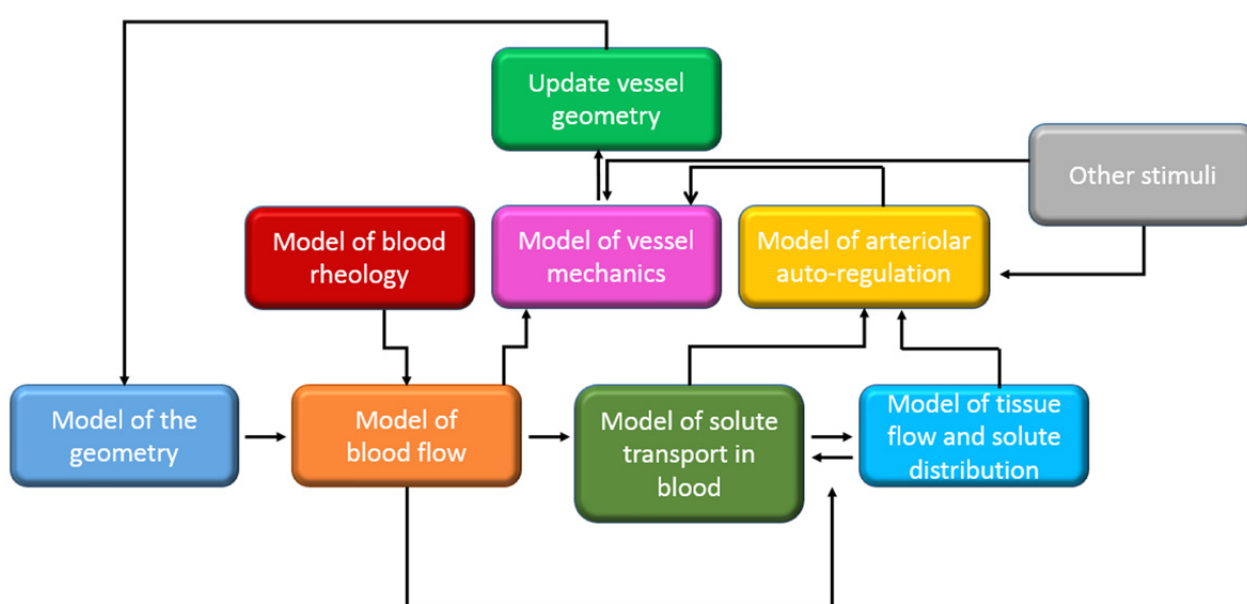


Figure 2. Main steps for developing mathematical models of the microcirculation. Arrows denote the directional flow of data. The geometry of the network defines the mathematical domain of the problem. The fluid dynamics (blood flow) and blood rheology models are combined with the network geometry to predict the distribution of flow, pressure, and hematocrit throughout the network. The fluid-dynamics action alters the vessel geometry exerting stresses on the vessel wall. Solute transport is studied along the vascular network, using the computed convective field. Solute is exchanged with the surrounding tissue, often according to a filtration model which depends on the difference of partial pressure of the solute across the vessel wall (double arrow symbol). In some models, especially the ones related to the exchange of large molecules, the fluid-dynamic pressure field may also enter in the solute exchange dynamics. Solute levels as well several other stimuli (neural, mechanical) contribute to autoregulation processes in the arterioles. Vessel geometry may thus vary due to the input of autoregulation and to the passive interaction with the blood flow (fluid-structure problem). The updated geometry enters back into the global model.

Theoretical modeling of microvascular networks typically involves several steps (see Figure 2). First, the geometry of the network must be specified. In this step, the length and diameter (or cross-sectional shape) of vessels are defined as well as the network connectivity. Next, fluid dynamics and blood rheology models are combined to predict the distribution of flow, pressure, and hematocrit throughout the network. Then, solute transport and delivery to the surrounding tissue is studied along the network. Vessel geometry may vary due to the interaction with the blood flow (fluid-structure problem) or the input of autoregulatory signals. Last, computed solute levels and other stimuli (neural, mechanical) may enter into the model of vessel regulation.

Several review articles address theoretical modeling of the microcirculation (recently, we refer to [12–15]). But, most of these papers focus on a specific aspect of modeling or on a specific scale of the problem. The aim of this work is to survey the mathematical approaches used broadly to study the microcirculation. Modeling microcirculatory networks requires *ad hoc* approaches. There are profound differences between modeling large/medium-sized blood vessels (e.g., the aorta, the circle of Willis, the femoral vessels) and modeling microcirculatory vessels. The number of vessels (a few vs. several thousand), vascular radial dimensions (cm vs. microns), the characteristic Reynolds and Womersley numbers (relevant vs. very low), and the role of blood rheology (Newtonian vs. corpuscular fluid models) are just some of the elements that impact the choice of mathematical and numerical models.

The present work is organized as follows. In Section 2 we review the definition of the geometry of microvascular networks and their surrounding tissues; in Section 3 we review models for blood flow when blood is modeled as a continuum or a corpuscular medium; in Section 4 we review models for gaseous solute transport in blood and delivery to tissue; in Section 5 we review models for vessel mechanics and autoregulation; in Section 6 we highlight models of the retinal microcirculation. Finally, in Section 7 we summarize the conclusions of our work and present perspectives on mathematical models in this field.

2. Modeling of Microvascular Networks and the Surrounding Tissue

Microvascular networks are very complex structures, and their complexity is often related to the tissue they are supplying. For example, the mesenteric microcirculation exhibits a fairly regular organization whereas the cerebral microcirculation differs greatly among subjects and within specific parts of the brain. In general, micro-vessels do not form precise arrays in the tissue; rather, their spacing is non-uniform and their pathways are often tortuous [15]. Different mathematical methods are chosen to describe the geometrical features of the different microcirculatory beds, where the degree of complexity included in the model depends on the environment being modeled.

2.1. Modeling of blood vessels

Despite the irregularities in network structure, almost ubiquitously, arterioles and venules are organized in tree-like structures and capillary beds in net-like structures. Arterioles and venules are thus analyzed with distinct models from capillaries. Vessels are generally classified as arterioles/venules or capillaries based on diameter. Within these classifications, vessels are often divided into more specific subclasses with explicit diameter ranges [16,17]. The number of vessels in a certain class or subclass may dictate the type of model used to describe that class. For example, in

complex 3D geometries with thousands of vessels, capillaries can be represented in a simplified manner to reduce the computational cost [18,19]. The modeling choice may also reflect the resolution limit of available imaging techniques. Last, but not least, since microvascular beds are the main site of metabolic exchange, it is also important for models to account for the tissue environment in which the microvessels are embedded.

2.1.1. Arteriolar and venular trees

We define two main types of arteriolar and venular tree models: (i) *compartmental models*, in which there is no topology (or connectivity) of the vessel branches, and (ii) *topological models*, in which a proper, connected, anatomical network is built according to geometrical data. Compartmental models maintain a low number of unknowns and are capable of reproducing the global behavior of the system. The more complex topological models account for the spatial distribution of field variables and the complexity of interactions among vessels in the microcirculatory network.

In the compartmental approach, several authors exploit the analogy of a vascular network with an electric circuit, formed by lumped resistive, capacitive and inductive elements. This reduced modeling approach allows for the inclusion of the microcirculatory network within a more comprehensive system, as in whole brain circulation studies [20,21]. Other compartmental models represent the arteriolar and venular trees as idealized classes of different hierarchy; for example, compartments are defined for large arterioles, small arterioles, capillaries, small venules and large venules [22]. The vessels comprising each compartment are arranged in parallel and are assumed to exhibit identical properties. The compartments are connected in series by conservation laws, so that each flow pathway from the arterial inflow to the venous drainage is equivalent. The functional characteristics of complete vascular beds are then derived, in an averaged sense, from the properties of the individual vessel classes and the number of vessels within each class.

In the topological approach, anatomically-specific geometrical data are used to build the model. Usually, the tissue is represented as a simple volumetric shape (e.g., cube, parallelepiped, cylinder) of linear dimension ranging from a hundred microns to a few millimeters. The main complexity resides in the representation of the embedded vessel network. According to a “topological geometrical” approach, vessel trees are constructed *ex-novo* using a mathematical algorithm that retains the relevant vascular morphology and topology. Principles of fractal geometry derived from Murray’s law have been used in [23,24] to define the diameter of daughter vessels sprouting from a bifurcation. The degree of asymmetry of the network can be controlled via an asymmetry parameter as in [25,26] or using distributions of generation numbers using, for example, the Horton-Strahler approach as in [27,28]. Stochastic growth techniques have been adopted to obtain random graphs (see [1], Ch.1, for a review), including the diffusion limited algorithm used in [29] to obtain a network with a prescribed fractal dimension. In the “topological anatomical” approach, the network geometry (vessel radii and lengths) is extracted from digitized images of experimental measures. A relevant problem is constituted by the reconstruction of the graph connectivity. Generally, a backbone system of vessels is identified (see the procedure detailed in [19]). Semi-automatic or manual techniques are then used to segment the backbone and prune dead-end vessels. In [30], intravital microscopy was used to define the vessel lengths and connection patterns in the mesenteric plexum. Vessel diameters were measured manually at the center of each segment. In [17], raw data

were obtained from a multi-diode target camera of rodent mesentery. Network connectivity, topology and diameter distribution were manually reconstructed from the images, and a Bézier approximation was used to enhance the segment tortuosity.

Over time, the resolution limits of various imaging techniques have vastly improved. For example, adaptive optics and ultra-high resolution optical coherence tomography has allowed for ultrahigh 3D resolution ($3 \times 3 \times 3 \mu\text{m}^3$) to capture data on the smallest capillary vessels. However, details of the smallest capillary vessels have not always been possible to obtain, and thus several models include artificially generated geometrical trees to account for these small vessels. For example, in [31], a 3D model of a $3 \times 3 \times 3 \text{ mm}^3$ portion of the human brain secondary cortex was presented. A backbone of visible large microvessels was reconstructed from high-resolution images, and smaller artificially generated segments were successively added using constructive optimization techniques. In [32], a network was obtained from high-resolution images of the mouse primary somatosensory cortex, ranging from the pial vessels to individual brain cells. In [16], images of the eye fundus were acquired and arteriolar vessels of the retina were segmented. Terminal arterioles with outlet diameter greater than 30 microns were connected with asymmetric structured fractal trees representing smaller vessels. Mixed topological/compartamental models were used by some authors to describe in detail certain portions of the network and, at the same time, represent other portions of the network in a lumped manner. For example, in [33], upstream and downstream portions of an otherwise microvascular anatomically accurate network were modeled by large arteries/veins and large arterioles/venules classes. In [20], lumped arteriolar/venular networks were coupled with more detailed models of larger vessels.

All topological networks are eventually reduced to graphs for computational purposes. The network graph is uniquely described by the node coordinates and by the connectivity matrix. In the latter, the (i, j) -th element is equal to one if node i is connected to node j and zero otherwise, leading to the creation of one “arc”. A single vessel can be composed of several arcs arranged in cascade or by a single arc. Vessel junctions are nodes at which different vessels are connected to each other. The most frequently adopted type of junction is the bifurcation (see the discussions in [18] and in [34]).

2.1.2. Capillaries

Capillary beds are composed of an extremely large number ($>10^4$) of tiny vessels (diameter ranging from 5 to 9 microns). Representations of capillaries using a vessel-by-vessel description are technically feasible but would be restricted to a small tissue region [30,33]. In certain topological geometrical models, capillaries are arranged as a compartment of parallel vessels, as in [23]. However, this representation does not fully describe the real net-like organization of capillaries. To model the net-like structure of capillary beds, some studies use mathematical algorithms to generate coherent capillary meshes. In [17] and [35], the capillary beds were generated on the basis of a Voronoi tessellation. In [27], a concentric circle mesh-like model was proposed to simulate capillaries in the rat retina. In [34], statistical algorithms were used to explore how the structural properties of the capillary bed influence the transport of blood through the human cerebral microvasculature. Sprouting angiogenesis algorithms are often used to generate capillary networks embedded in tumoral tissues (see, e.g., [36–39]). The network shape is forged by stimuli coming from the tumor itself.

2.2. Tissue

Unlike large blood vessels, microcirculatory vessels are embedded within tissues. This enables communication and mass (fluid, solute) exchange between the parenchymal tissue and these vessels. Several models thus couple a tissue description with the microcirculatory network. In compartmental models, the tissue is described as a well-mixed medium exchanging mass flux with the circulatory network across a lumped boundary. In topological models, the surface of exchange is extended and geometrically characterized. In general, the tissue slab is assumed to have a simple geometrical shape, for example a cylinder or a parallelepiped. The volume of the considered tissue slab may range from a few mm^3 to several hundred mm^3 . There are also more complex representations. For example, in [40], the intricate geometry of lung alveoli is considered, where the capillary plexi surround an assumed spherical tissue region. In [18], the tissue continuum consists of nodes interconnected on a lattice, each node representing a tissue voxel with associated numerical quantities. Some authors introduce separate representations for the interstitial portion of the tissue and the (metabolically active) parenchymal cellular portion, see, e.g., [41].

2.3. Homogenized models: perfused-tissue representations

In some studies, mathematical techniques are used to homogenize the tissue and embedded vessels as single medium. Such techniques are typically employed when describing the capillary-perfused tissue matrix, for which the network of vessels is so dense that the computational cost of addressing each vessel is too high. A simple model of capillary-perfused tissue can be found in [42] where capillaries were represented as distributed sources in the homogeneous tissue. More sophisticated homogenized models give rise to porous media representations. Effective permeability and diffusion coefficients of the matrix were computed via different approaches. For example, in [18], a number of sub-volumes (cells) were identified in the capillary plexum. For each cell, integral quantities such as effective conductance, vascular volume, and surface area were determined via explicit computation. Upscaling techniques are successively used to connect the homogenized medium to larger scale vessels. Homogenization techniques are widely used to study blood perfusion in tumoral tissues. The literature in this field is very vast and in this context we limit ourselves to cite the comprehensive review works [43–46].

In Tables 1 and 2, we compare geometrical descriptions of the microvascular bed for compartmental, topological and homogenized approaches. We do not include purely morphometric studies (for which we refer to [17]) and we limit ourselves to relevant examples of a certain type of model, giving preference, when possible, to 3D models. The Tables in this review provide a comprehensive list of studies that are not all referenced in the article due to space constraints.

3. Modeling the Fluid Dynamics of Blood

Blood is a dense suspension of cells in plasma solvent. Red blood cells (RBCs) are the primary cellular constituent of blood, with a volume fraction (hematocrit, H_D) of typically 40–45%. While plasma is a Newtonian fluid, interactions between cells and plasma lead to complex non-Newtonian dynamics. This is especially true in the microcirculation, since vessel dimensions are comparable to cell diameter [13]. Radial migration of the RBCs away from the vessel wall occurs from

hydrodynamic interactions, forming a low-hematocrit/cell depleted layer along the vessel wall [68]. This phenomenon is the basis of several important rheological effects observed *in vitro* and *in vivo* [17]: (i) the Fåhræus effect, which is the apparent reduction in tube hematocrit with respect to discharge hematocrit [69,70]; (ii) the Fåhræus-Lindqvist effect, which dictates that the apparent viscosity of blood decreases when the vessel diameter is reduced below 1 mm; and (iii) plasma skimming at network bifurcations (also known as the “network Fåhræus effect”), in which the fraction of the total RBC flow in the mother vessel of a bifurcation that enters one of the daughter branches does not correspond to the fractional blood flow entering that branch, due to the hindrance of the cell depleted layer. Plasma skimming results in a heterogeneous spatial distribution of hematocrit in the network [71].

Table 1. Geometric description of compartmental models (R = resistive, C = capacitive, L = inductive element in electric analogy).

Reference	Species and district	Microcirculatory compartments	Other compartments	Tissue
Ye (1993) [47], Arciero (2008) [22], Piechnik (2008) [48], Fantini (2014) [49]	human	[47]: arteriole and venule compartments grouped in length classes, capillary compartment; [22]: representative segment model: large/small arterioles and venules and capillaries; [48]: different hierarchies of arteriolar/venular vessels {Fantini, 2014 #67}: arteriole, capillary and venule compartments;	[22]: large inlet/outlet artery/vein	[47],[49]: lumped tissue compartment
Ursino (1998) [50], Spronck (2012) [51], Payne (2006) [52], Diamond (2009) [53], Müller (2014) [54]	human brain	[51]: PCA arterioles (R-C); [50]: large and medium/small pial arteries (R-C); [53]: cerebral arterioles and capillaries (R-C); [54]: arterioles/capillaries/venules (R-C-L) attached at the terminals of larger vessels; [52]: arterial and capillary/venous compartments (R-C)	[50]: cerebral arteries and veins, CSF; [51]: PCA + venous, [53]: pial arteries/veins, body circulation, CSF,ISF;) [54]: body circulation, large brain arteries and veins	-
Gutierrez (2004) [55], Vazquez (2008) [56], Barrett (2013) [57]	[55]: dog limb; [56], [57]: human brain	[55],[56]: unique vascular compartment; [57]: arteries, capillaries and veins		lumped tissue compartment

Table 2. Geometric description of topological models (A = anatomical, G = geometrical).

Reference	Dimension and district	Arterioles	Venules	Capillaries	Inlet/Outlet	Tissue
Liu [16] (2009)	2D human eye	A + G for smaller vessels		G	1 main inlet and 12 outlets	as boundary condition
Guibert (2010) [19]	3D human brain	A	A	G (2D mesh)	multiple I/Os	
Fang (2008) [58], Reichold (2009) [18], Lorthois (2011) [59], Pan (2014) [30]	[58], [18]: 3D rat cortex, [59], [52]: 3D human brain; [30]: 2D, rat mesentery	A	A	A	[18]: pial arteriole, draining venule; [30]: 1 main artery/vein, 30 secondary inputs and 4 secondary outputs	[58]: $230 \times 230 \times 450 \mu\text{m}^3$ region, [18]: $0.23 \times 0.23 \times 0.45 \text{ mm}^3$ region [59]: 1.6 mm^3 region
Fry (2013) [33]	3D, hamster cremaster Muscle	A smaller arterioles + G large arterioles	A smaller veins +G large veins	A	1 main artery and 2 veins, 6 terminal arteries	3D parallelepiped
Gould (2015) [17]	3D, human brain	A + G for smaller vessels	A + G for smaller vessels	G (Voronoi tessellation)	1 main artery and 1 main vein	27 mm^3
Boas (2008) [60]. Takahashi (2014) [61]	[60]: 1D human brain ; [61]: 1D	G	G	G	1 main artery and 1 main vein	
Ganesan (2010) [62]	3D rat retina	A	A	G (2D mesh)	6 main arteries and 6 main veins	
Causin (2016) [29]	3D human retina	DLA algorithm	DLA algorithm	G (equivalent resistance)	1 main artery and 1 main vein	1D slabs ($250 \mu\text{m}$)
El-Bouri (2015) [63], Su (2012) [34], Safaeian (2013) [35], Gagnon (2015) [64], Tsoukias (2007) [65], Park (2016) [66]	[63], [34], [35], [58]: 3D human brain; [65]: 3D hamster cheek pouch retractor muscle; [64]: 2D brain;			G with [34] investigation of different approaches (shortest arc, Gamma distribution, spanning tree); [58]: minimum spanning tree; [35]: Voronoi tessellation ; [64]: hexagonal tessellation	[34]: two outlet and inlet junctions; [35]: twelve inlet and 24 outlet flows; [56]: 1 inflowing arteriole and 3 outflowing venules; [65]: 2 arteriolar inlets and two venous outlets; [66]: multiple I/Os	[63]: cubes with side from 125 to $625 \mu\text{m}$; [34]: cube with side $10 \mu\text{m}$; [35]: $0.6 \times 0.38 \times 0.3 \text{ mm}^3$ region; [65]: $100 \times 100 \times 800 \text{ mm}^3$ region
Gorodnova (2016) [67]	3D	G (directed force layout algorithm)	G (directed force layout algorithm)	G (fractal)	1 inlet and multiple outlets	sphere of radius of 0.6 cm

3.1. Continuum modeling of blood flow

Blood flow in the microcirculation differs substantially from flow in large vessels. In the microcirculation, inertial effects as well as pulsatility are generally neglected (see [72] for exceptions). A large majority of blood flow models applied to the study of networks treat blood as a (multiphase) continuum. In the simplest approach, whole blood flow is described as the flow of a Newtonian fluid governed by the Stokes equations. Poiseuille's law has been traditionally used as a first approximation of such equations. In this context, the volumetric flow Q in the vessel is proportional to the pressure drop ΔP along the vessel and the fourth power of the vessel radius R :

$$Q = \frac{\pi}{8} \cdot \frac{R^4 \Delta P}{L \mu} \quad (1)$$

The symbol μ in Eq. 1 is the whole blood viscosity. In comprehensive models of the circulatory system, μ is generally prescribed as a constant [54] (see also [59] for the same choice in a smaller network). More physiologically-relevant expressions for μ have been obtained from empirical equations fitting the Fåhræus and Fåhræus-Lindqvist effects to a range of hemodynamic measurements [15]. As reviewed in [73,74], *in vitro* data were originally used to determine a relationship between effective viscosity, hematocrit and glass-tube diameter. This relationship was subsequently modified based on data that showed a greater *in vivo* resistance. Specifically, μ corresponds to the concept of bulk ("apparent") viscosity and is formally obtained from experimental data and upon application of the Hagen-Poiseuille model as:

$$\mu_{app} = \frac{\pi}{8} \cdot \frac{R^4 \Delta P}{LQ} \quad (2)$$

Often, the relative value of the apparent viscosity (*i.e.*, normalized with respect to plasma viscosity) is provided. Recently, an improved model of viscosity has been devised by including the effects of the endothelial surface layer (ESL) [74]. Alternative models for the viscosity have been proposed in [75], where an empirical equation for the apparent relative viscosity was derived as a function of hematocrit, and in [23], where an expression for μ as a function of radius was proposed (see also [76]). Further attempts to develop physically consistent constitutive models of blood viewed as a non-Newtonian fluid have led, for example, to the use of the Casson-Quemada model, where the viscosity depends on the shear rate (we refer to [77] for a comparative study of different constitutive equations).

The hematocrit value appearing in the phenomenological relations for the viscosity may be prescribed as in [16] or can be treated as an unknown in the model, as done in [31,62,78]. When the hematocrit is computed, an additional equation for the mass conservation of the continuum fluid representing RBCs must be added to the system, and volume fractions for plasma and RBC phases must be taken into account according to mixture theory [79].

When modeling a network of vessels, an analogy to Kirchhoff's first rule for electrical networks is generally adopted at the vessel bifurcations, where flux and RBC flux mass balances are enforced (see [62] for a detailed discussion of the related numerical procedure); pressure continuity is also usually enforced at bifurcation nodes [60]. Due to the low Reynolds number of the flow in microvessels, the continuity of the static pressure at bifurcations is generally used instead of the

continuity of the total (static plus dynamic) pressure (see [80] for a discussion on this issue and [30] for an example where the continuity of the total pressure is considered). In a microvascular network, a proper treatment of plasma skimming at the bifurcations is also needed. Empirical equations have been developed that depend on the flow split in the bifurcation, the vessel diameters, and the discharge hematocrit in the parent vessel in [74,81]. An alternative approach that can be applied to branch points with more than two outflowing segments was proposed in [17]. Another alternative approach has been proposed based on the assumption that the distribution of RBCs in diverging bifurcations satisfy a mathematical principle of optimality [69].

A mathematically rigorous approach for computing blood flow in a vessel stems from the mathematical procedure of averaging the velocity field (approximated by a purely axial component) over the vessel cross section. Namely, introducing a system of cylindrical coordinates (r, θ, z) and assuming that the variables are separable, one sets

$$u = \bar{u}(z)f_u(r) \quad (3)$$

where \bar{u} is the average velocity on the cross section A , such that $Q = A\bar{u}$, and where f_u is a prescribed radial shape function. A typical velocity profile is given by the function [82]

$$f_u(r) = \frac{\gamma+2}{\gamma} \left[1 - \left(\frac{r}{R} \right)^\gamma \right] \quad (4)$$

where γ is a bluntness parameter ranging from 2 (parabolic profile) to 9 (plug flow profile). This approach allows for a rigorous asymptotic analysis of the various contributions arising in the balance equations.

To obtain a unique solution for the fluid-dynamic fields in the network, it is necessary to impose (i) flow or pressure boundary conditions on inflowing and outflowing segments and (ii) hematocrit boundary conditions on inflowing segments. Difficulties may arise when multiple inflows/outflows exist but the corresponding boundary conditions are not all available from experiments. Several approaches have been used to address this issue. The use of literature-based typical values at outflow under the satisfaction of “target constraints” is the basis of the approaches proposed in [83]. A parametric analysis of boundary condition values has been carried out as well in [83] and [59].

An immediate extension of the homogeneous continuum was originally proposed in [84] and further developed in several works. In these approaches, the domain is usually a single cylindrical vessel in which two layers are arranged in a concentric fashion: an external plasma region (denoted here below by ‘ a ’) devoid of cells and a core RBC region (denoted here below by ‘ c ’). Each layer is generally supposed to consist of an incompressible Newtonian fluid with constant viscosity (μ_a in a and μ_c in c , usually $\mu_c > \mu_a$). Imposing the balance of mass and momentum in each fluid domain with appropriate interface boundary conditions (continuity of velocity and shear stress are usually enforced [85,86,87]) yields two distinct velocity profiles of the type

$$v_a = \frac{\Delta P}{L} \frac{1}{4\mu_a} (R^2 - r^2), v_c = -\frac{\Delta P}{L} \left(\frac{r^{*2} - r^2}{4\mu_c} + \frac{R^2 - r^{*2}}{4\mu_a} \right) \quad (5)$$

where r^* is the (unknown) thickness of the cell depleted layer (see, e.g., [88] for a simplified trial-and-error solution procedure to determine its size). The above relations for the core and cell depleted layer velocities have been again generalized to the case of blunted velocity profiles [89]. The overall mass balance of RBCs in the tube is then defined by:

$$QH_D = 2\pi \int_0^R v(r)h(r)rdr, \quad (6)$$

where $h(r)$ is the radial profile of the hematocrit, commonly chosen to be equal to zero in the cell depleted layer and equal to the (unknown) core hematocrit in the RBC layer [86]. Generally, the core hematocrit is assumed to be constant, but polynomial radial profiles [84],[90] have also been proposed. In [91], the RBC core was divided into two domains: an outer region characterized by reduced hematocrit with a constant or linear radial profile and linear variation of viscosity, and a core region with uniform hematocrit concentration and uniform viscosity. To compute the unknown quantities, model closure is performed in the above models using empirical data. For example, in [86], the core viscosity is described as a function of hematocrit via phenomenological equations using the model described in [71] or [92]. In some studies, the Oldroyd-B [93] or Casson [83] models have been used to describe the RBC core phase as a non-Newtonian fluid. In [89], a detailed derivation of the velocity profile in the core region considering a power-law fluid model is carried out.

3.2. Mesoscale modeling of blood flow

While a continuum description of blood is sufficient to obtain flow data for blood viewed as a bulk volume, more detailed studies are needed to consider the corpuscular nature of blood. Studying such details will aid the comparison and analysis of the mechanisms that lead to experimentally observed results of blood rheology. These approaches are known in the specialized literature as “mesoscale models”. Here, we limit ourselves to a brief description of the main approaches found in mesoscale models and we refer for additional details to the recent specific reviews by Cristini et al. [68] (till 2005), Secomb et al. [94] (till 2011), AlMomani et al. [95] (till 2012), Ju et al. [96] (till 2015) and Ye et al. [97] (till 2016).

3.2.1. Modeling of the cellular phase

Red blood cells are the most abundant type of cells in blood. An adequate representation of their mechanical and rheological properties requires correct descriptions of the elastic and viscous properties of their membrane, the bending resistance of the membrane, and the difference in viscosity between the external and internal fluids. Deformable RBCs were first modeled with simple elastic models that evolved into hyperelastic models for fully deformable 3D cells. Both discrete and continuum models of the RBC membrane have been proposed. Discrete spring network models have been widely used to model the RBC membrane (see, e.g., [98,99]). A discrete representation of the membrane as a network of viscoelastic springs in combination with bending energy and constraints for surface-area and volume conservation is adopted for example in [100]. The continuum approach treats the whole cell as a homogeneous material represented by appropriate constitutive equations. Several models adopt the Mooney-Rivlin or Skalak constitutive relations, eventually adding bending resistance [101]. More complex constitutive equations, accounting for shear-thinning and viscoelasticity, have also been proposed (see, e.g., [102]). Mixture-type “biphasic models” as well as two-phase models of the cell as a deformable capsule with liquid cytoplasm enclosed by an elastic or

viscoelastic membrane have been used to represent the multiphase nature of the cellular components [103–107]).

The number of RBCs being modeled dictates the numerical approach. Ye and colleagues developed a series of papers where a single RBC is considered (see [97] and references therein). This approximation is valid where RBCs move in single-file, namely in capillaries. More realistic simulations of multiple RBCs flowing through vessels with diameter ranging from 10 to 500 microns remains a major challenge. A large population (thousands) of RBCs is necessary to account for cell-cell hydrodynamic interactions in these vessels. Sun et al. [105] used a Lattice-Boltzmann discretization to describe blood flow (plasma with suspended rigid particles) in a 2D channel. In recent years, some authors have proposed the use of hybrid models to describe single cellular components and their interaction in combination with a continuum representation of intra-cellular and extra-cellular processes (see the works by Bessonov and colleagues, e.g., [108]).

A number of studies introduce mathematical models of other cellular components of blood, namely white blood cells and platelets immersed in plasma flow. Complex mechanisms involving these particles, such as coagulation and interactions between different types of cells, have also been studied. We refer to [109,110] for detailed overviews on these aspects. Moreover, we refer to [111] for an overview of the main mathematical models related to blood formation (hematopoiesis), disorders and treatments.

3.2.2. Modeling of the plasma phase

Lattice Boltzmann methods, mesh-free particle methods and dissipative particle dynamics (DPD) have been used to discretize the plasma component of blood. We refer to [112] for a detailed overview of these approaches and discussion of their applicability to problems of different scales.

3.2.3. Modeling of cell-to-cell interactions

RBCs immersed in plasma flow aggregate and form rouleaux due to mutual interactions. The equilibrium configuration and the cell shape are related to the strength of these interactions. Intercellular interactions and cell aggregation have been modeled using a Morse potential [113], according to a ligand-receptor binding model [114,115] or using a theoretical formulation of depletion energy [96].

3.2.4. Modeling of plasma-cell interactions

The motion of the RBC membrane is coupled to the flow of the surrounding plasma, thus yielding a fluid-structure interaction problem. The difficulty of such a problem lies in the fact that RBCs can approach each other very closely, till aggregation. Moving mesh approaches are thus not frequently used, since meshes may face break down. The immersed boundary method has been a popular approach in combination with a fixed Cartesian mesh for the fluid [116]. Mesh-free particle methods have also been used where fluid-structure interactions are dealt with by adding elastic forces to membrane particles (see, e.g., [117], with an application to malaria infection). We refer to [118] for a comprehensive review of the possible numerical approaches in this context.

Table 3. Models of blood flow in concentric regions (“a” = cell depleted layer, “c” = RBC core).

Reference	Cell-depleted layer fluid model	Core layer fluid model	Hematocrit model	Viscosity model
Sharan [86] (2001) [88]	Newtonian fluid, Poiseuille flow	Newtonian fluid, Poiseuille flow	constant in c, zero in a, relation between tube hematocrit and core hematocrit from Pries’ model	model from Pries
Verma (2014) [89], Zaman (2016) [93], Shaw (2014) [119], Sriram (2014) [69], Das (1998) [90]	Newtonian fluid, Poiseuille flow	axial flow; [89], [121]: power law fluid; [93]: Oldroyd-B fluid; [119]: Casson fluid with glycocalyx layer; [69], [90]: Quemada fluid	[89]: constant in c, zero in a, parametric analysis, [93]: no hematocrit; [119]: given constant in c; [69]: constant in c, zero in a; [90]: polynomial expression in c and small value in a.	[89]: prescribed constant values; Zaman: prescribed relaxation and retardation parameters; [119]: constant in a, Pries model in c; [69]: constant in a, fitted from data in c; [90]: analytic expression function of hematocrit
Chebbi (2015) [88]	Newtonian fluid, Poiseuille flow	Newtonian fluid, Poiseuille flow	constant in c, zero in a, plasma skimming model (bifurcation)	constant value

3.3. Blood flow in homogenized tissue-perfused models

The idea of explicitly modeling arteriolar and venular trees and using homogenization techniques to describe the capillary-perfused tissue is the focus of several studies. The concept of a capillary-perfused tissue relates to the theory of porous media. Fluid flow in this composite matrix is studied introducing effective permeability and diffusion coefficients. Several approaches have been proposed to compute these quantities, ranging from model unit cells [18] to asymptotic analysis [120]. Double porosity media have also been proposed in this context. In these models, a fracture pore system represents the embedded capillaries while a less permeable matrix pore system represents the interstitial fluid space [40].

4. Models of Gas Transport in Blood and Tissue

The circulatory system is responsible for the transport, delivery and waste removal of gaseous species from blood to every tissue in the body. Oxygen, for example, is delivered to tissue via passive diffusion from blood, so blood must flow within a very short distance of every tissue point in the body. The distance that oxygen can diffuse into tissue is on the order of microns, and thus the circulatory system plays a critical role in transporting blood throughout the body via convection along a network of vessels before reaching the capillaries where the majority of diffusive oxygen exchange occurs. Blood gas transport involves a combination of convection, diffusion, permeation,

and/or chemical reactions and takes place over a range of spatial and temporal scales (see [15,121] for recent physiological reviews). The structural complexity and heterogeneity of the vascular networks of the microcirculation leads to heterogeneity also in tissue oxygenation and consumption. Experimental measures of the impact of such heterogeneity on tissue oxygenation are difficult to obtain, and thus theoretical modeling has served as an essential tool to characterize the physiological implications of such heterogeneity on oxygen delivery to tissue. Numerous theoretical models have been developed to describe the transport of oxygen to tissue by the microcirculation. These models include either steady-state or time-dependent oxygen transport descriptions from single or multiple vessels, as reviewed previously [122,123].

The value of theoretical models in providing a quantitative understanding of organ function at homeostasis and in pathological states such as ischemia and hypoxia has long been recognized. Studies of gas transport from blood to tissue date back to the pioneering work of Krogh [124] in 1919, and were mainly focused on O₂ transport. These studies sought certain quantities of interest: (i) tissue O₂ extraction fraction (OEF), defined as the weighted average inlet-outlet gas concentration, which is an important indicator of tissue viability; and (ii) (cerebral) metabolic rate of O₂ ((C)MRO), which correlates BF and the metabolic rate of O₂ consumption. We refer to [125] for a precise definition of these quantities and their inter-correlation. As established more recently, these two definitions are not sufficient for estimating tissue oxygen (gas) levels since the heterogeneity of the microcirculation leads to heterogeneity in gas gradients, chemical interactions among species, and the spatial distribution of gas in tissue. This section reviews models of gas transport in tissue and blood. We do not consider models devoted to the study of BOLD (blood-oxygenation level dependent) signals in medical imaging, for which a vast literature exists. We refer for this topic to [83,126] and references therein.

4.1. Modeling gas transport in tissue

4.1.1. Krogh cylinder model

The Krogh cylinder model [124] defines an array of parallel, evenly spaced oxygen-delivering vessels (e.g., capillaries) that supply oxygen exclusively to tissue cylinders surrounding each vessel. In this model, tissue oxygen consumption is assumed constant, the tissue partial pressure of oxygen ($P_{O_2}^T$) at the capillary wall equals the average capillary PO₂, axial diffusion of oxygen is neglected, and tissue oxygen solubility and diffusivity are uniform. Eq. 7 gives the partial differential equation for the partial pressure P_i^T of species i in the cylindrical tissue surrounding a capillary:

$$0 = -D_i^T \left(\frac{1}{r} \frac{\partial}{\partial r} \left(r \frac{\partial P_i^T}{\partial r} \right) \right) + \dot{R}_i^T, \quad (7)$$

where r is the radial coordinate and D_i^T and \dot{R}_i^T are the constant tissue diffusivity and source/consumption rate (possibly depending on other chemicals), respectively. An explicit solution of Eq. 7 can be found using a Bessel function expansion that gives the radial variation in tissue gas partial pressure as a function of radial distance from the vessel. Although the model includes many simplifications and often does not yield predictions that are consistent with experimental measures, the Krogh model provides an important foundation in the study of oxygen exchange with tissue and has been used and improved upon by several models.

The Krogh model has been extended to include other effects including time-dependent transport [127], $P_{O_2}^T$ -dependent O_2 consumption (e.g., Michaelis-Menten kinetics) [128,129,130], myoglobin-facilitated tissue transport and intravascular resistance to radial oxygen diffusion. Myoglobin (Mb) can bind and release oxygen in the same way as the hemoglobin molecule, and thus movement of myoglobin can increase oxygen diffusion (known as myoglobin facilitation). In several models, the term for total oxygen flux is altered to include the effects of Mb facilitation [131,132,133], and the models predict that this extra term provides tissue with some resistance to hypoxia by increasing oxygen diffusion to low- PO_2 regions. Capillary intravascular resistance arises from the PO_2 drop between the center of a red blood cell and the capillary wall and has been shown to depend on capillary diameter and red blood cell velocity [78,134]. This factor can also be approximated in models by using a flux boundary condition on tissue PO_2 at the outer edge of the capillary wall instead of the continuous PO_2 condition of the Krogh model. Detailed reviews about the Krogh model and its applicability in standard and modified formulations are provided in [122,123,135,136].

4.1.2. Compartment models

An alternative, yet related, simplified approach is represented by well-stirred compartment models, in which the tissue is characterized by a single, uniform compartmental concentration/pressure. The compartmental equation in the tissue can be formally obtained from 3D balance equations, performing volume averaging, yielding:

$$V^T \frac{d\bar{P}_i^T}{dt} = \sum_m k_m (\bar{P}_i^m - \bar{P}_i^T) + \dot{R}_i^T, \quad (8)$$

where bars indicate average values, V^T is the tissue compartment volume and exchange with other compartments (including blood and a possible subdivision in interstitial and cell phases) with concentration \bar{P}_i^m is considered. This procedure and its connection with the Krogh model are outlined in [137].

Recent models of gas delivery adopt a fully spatially-dependent description of the gas content in tissue, where diffusive processes occur due to spatial gradients. In [42], the concept of “capillary-perfused tissue” is introduced, in which the tissue description is enriched with terms representing gas exchange with embedded capillaries. Porous medium approximations of the tissue carried out in [18,138], where a seepage interstitial velocity computed from a Darcy model conveys the gas, are conceptually similar though mathematically more involved.

4.2. Modeling gas transport in blood

A prototype molar balance in blood for a generic gaseous species i is formulated in [139], according to the following partial differential equation:

$$\frac{\partial c_i^B}{\partial t} + v_B \cdot \nabla c_i^B - D_i \Delta c_i^B = \dot{R}_i^B, \quad (9)$$

where v_B is the advective blood velocity (consistently computed, see Section 3 or prescribed), D_i^B the gas diffusion coefficient in blood and \dot{R}_i^B the reaction transform rate in blood. The gas content

(dissolved component) C_i^B and its partial pressure P_i^B are related according to Henry's law $P_i^B = C_i^B / \alpha_i$. In compartmental approaches, for example [50,55,140], Eq. 9 reduces to

$$\frac{\partial \bar{C}_i^B}{\partial t} + Q [\bar{C}_{i,in}^B - \bar{C}_{i,out}^B] + \sum_m k_m (\bar{C}_i^m - \bar{C}_i^B) = \dot{R}_i^B \quad (10)$$

In [22,139,141], multiple vessel compartments are considered, and thus Eq.10 also includes the cascade of gas from one vessel hierarchy to the next.

When dealing with a spatially resolved form of Eq. 9, as with blood flow models, a radial gas concentration profile is prescribed via cross-sectional averaging. A mathematical characterization of this procedure can be found for a generic solute in [142] and specifically for O₂ in [29].

In Eq. 9, blood is treated as a single-phase continuum and the i -th gaseous species is characterized by a single partial pressure value. More generally, gases like O₂, CO₂ and NO are carried in blood in hemoglobin-bounded form and dissolved form. A multi-phase model of blood (plasma dissolved and RBC-bound fractions) is a more suitable choice to represent a wider range of conditions. For example, for oxygen, the total concentration in blood can be written as

$$C_{O_2,tot} = \alpha_{pl,O_2} P_{pl,O_2} (1 - H_{D,O_2}) + \alpha_{RBC,O_2} P_{RBC,O_2} H_D + c_{Hb,O_2} H_D S, \quad (11)$$

where the subscript pl indicates the fraction dissolved in plasma and the subscript RBC indicates the fraction dissolved in the RBCs; where H_{D,O_2} and $(1-H_{D,O_2})$ are the hemoglobin bound and free fractions, respectively; and where c_{Hb,O_2} is the hemoglobin carrying capacity for oxygen. Typically, the free part in the plasma and the free part in the RBCs are assumed to be at the same partial pressure, so that $P_{pl,O_2} = P_{RBC,O_2} = P_{O_2}^B$. Also, local chemical equilibrium is usually assumed for the free and bound fraction of the gas. This introduces a saturation function $S = S(P_{O_2}^B)$, connecting the partial pressure of free and bound gas fractions. The most common function used to describe saturation is the Hill equation, which supposes a single-step reaction kinetic for O₂ binding to Hb. A few models assume non-equilibrium kinetics, as in the Adair equation (see [121] for a complete discussion of this topic). In non-equilibrium conditions, separate balance equations are written for the bound and the dissolved fractions that include reaction terms between the different forms (see [78]).

In smaller vessels like capillaries, continuum-based approaches like the one in Eq. 9 may fail to yield accurate results. Approaches based on discrete modeling of RBCs address this issue. Generally, these models work in the frame of reference of the erythrocyte, which simplifies the numerical treatment of the reaction between oxygen and hemoglobin in RBCs. This idea was first used by [79], who used an analytical model with a cylindrical RBC and the adjacent tissue to compute MTCs. In [143], a model with concentric layers around the capillary for wall, interstitial fluid, and the tissue is presented. Recent contributions from this viewpoint can be found in [144].

Detailed mathematical models of the acid-base chemistry of blood based upon mass action and mass balance equations have been also developed (see, for example, [145]). Transport of other species (e.g., CO₂, CO, NO, etc) affects the transport of oxygen and is thus also an important modeling consideration. More precisely, CO₂ shifts the hemoglobin-oxygen saturation curve, CO competes with oxygen for binding sites to Hb, and NO inhibits mitochondrial oxygen consumption. Several studies have implemented such multi-species models, for example for oxygen and carbon dioxide [41,146–149]. Ye et al. [139] developed a compartmental model of oxygen-carbon dioxide transport in the microcirculation that uses a Krogh cylinder approach and accounts for the coupling

between oxygen and carbon dioxide transport. The equations for steady-state oxygen-carbon dioxide coupled transport in the microcirculation are given as:

$$Q[c_{i,g}(0) - c_{i,g}(L)] - E_{i,g}(P_{i,g}^B - P_{n,g}) - F_{i,g}(P_{i,g} - P_{n-i,g}) = 0, \quad (12)$$

for $i = 1, 2, \dots, n-2; g = 0, 1$

$$\sum_{j=1}^{n-1} E_{j,g}(P_{j,g} - P_{n,g}) + M_g V_T = 0, \quad (13)$$

for $i = n; g = 0, 1$

where $c_{i,g}$ is the average total concentration of gas ($g = 0$ for oxygen, $g = 1$ for carbon dioxide) over the vessel cross-section, M_g is the metabolic rate, V_T is the tissue volume, F_i is the countercurrent exchange of gas (omitted in the model), E_i is the diffusion conductance, and P_i is the partial pressure in the i -th compartment. The model predicts the distributions of PO_2 , PCO_2 , saturation, and pH within the vessel and tissue compartments and includes the Bohr effect and Haldane effect. The effects of the radial variation in PO_2 and PCO_2 and the difference between the metabolic rates of the vessel wall and tissue are included in the model to improve the accuracy of oxygen and carbon dioxide vessel-tissue conductance predictions. Overall, including the transport of multiple species significantly improves predictions of tissue oxygenation when compared with models including only transport of a single species.

4.3. Modeling blood-tissue gas exchange

Blood-tissue exchange occurs mainly in capillary beds, although arterioles are also sites of important gas exchange in some cases. For example, it has been observed that in the hamster retractor muscle, two-thirds of oxygen is exchanged in the arterioles and the rest in capillaries while cerebral cortical capillaries unload about twice the amount of oxygen to the brain tissue as compared to arterioles [42,150].

4.3.1. Fick's Law models

From a mathematical viewpoint, a straightforward representation of the exchange process prescribes a proportionality relation between gas concentration in different compartments (for example, between venous and tissue concentration [142,151] or between arteriolar and tissue concentration [152]). In these models, the transfer of gas through the vessel wall is defined according to Fick's law:

$$J = \Delta N / \Delta t = DA \Delta C / \Delta x = L_p A \Delta C \quad (14)$$

where $\frac{\Delta N}{\Delta t}$ is the amount of the gas substance exchanged per unit time, D is the diffusion coefficient for the substance through the vessel wall, A is the surface area available for diffusion, ΔC is the concentration difference across the vessel wall ($\Delta C = C_i^B - C_i^T$), Δx is the thickness of the vessel wall ($\sim 1 \mu m$) and L_p is the permeability of the capillary wall defined as $D/\Delta x$ [121]. The value C_i^T

can be a given, fixed, parameter or can be computed from a consistently coupled model for tissue as for example in [29,31,58,60].

In some approaches stemming from modifications of the Krogh model, a mass transfer coefficient (*MTC*) is introduced, defined as $MTC = \frac{\bar{J}}{\bar{P}_t^B - \bar{P}_t^T}$, where the bars indicate the average of the quantity per unit area of the vessel wall [123]. The *MTC*, which can be considered as a permeability of the wall appearing in Eq.(12) [122], relates the PO₂ drop from the intravascular space to the O₂ flux across the capillary wall. Since the *MTC* depends on hematocrit, prescribing it introduces the influence of RBC flow on tissue oxygenation. Occasionally, the *MTC* quantity is expressed as a function of the non-dimensional Nusselt [123] or Sherwood numbers [153].

McGuire and Secomb [132,133] developed a model of oxygen transport to exercising skeletal muscle that is an example of an extended Krogh model that includes the effects of the decline in oxygen content of blood flowing along capillaries, intravascular resistance to oxygen diffusion, and myoglobin-facilitate diffusion. The oxygen consumption rates depend on both convective and diffusive limitations on oxygen deliver when oxygen demand is high.

4.3.2. Green's functions model

Secomb et al. [154,155,156] introduced a steady-state model of oxygen transport in capillary networks and surrounding tissue based a Green's function method (Eqs. 15–17). The model utilizes techniques from potential theory which seek to reduce the number of unknowns needed to represent the oxygen field. Vessels are modeled as discrete oxygen sources, and the tissue regions are considered oxygen sinks; the resulting oxygen concentration at a tissue point is calculated by summing the oxygen fields (called Green's functions) produced by each of the surrounding blood vessels. The tissue is assumed homogeneous with respect to oxygen diffusivity (*D*) and solubility (α), and Eq. 15 is obtained from the conservation of mass where *P* is tissue PO₂ and *M*(*P*) is the tissue consumption rate (usually assumed as a constant value or according to Michaelis-Menten kinetics). The Green's function *G*(**x**,**x**_{*i*}) is the solution of Eq. 16 and represents the PO₂ at a point **x** resulting from a unit point source at **x**_{*i*}. The PO₂ is given by Eq. 17 where *q*_{*i*} represents the distribution of source strengths. A great benefit of this model is the ability to predict tissue oxygenation for a heterogeneous network of capillaries in three dimensions. The model predicted a much lower minimum tissue PO₂ than would be predicted by a corresponding Krogh model.

$$D\alpha\nabla^2 P = M(P) \quad (15)$$

$$D\alpha\nabla^2 G(\mathbf{x}, \mathbf{x}_i) = \delta(\mathbf{x} - \mathbf{x}_i) \quad (16)$$

$$P = \sum_i G(\mathbf{x}, \mathbf{x}_i) q_i \quad (17)$$

More detailed descriptions of the blood-tissue gas exchange are considered by some authors. They usually consider a single vessel and partition the vessel wall into three or four layers (endothelium, smooth muscle layer and adventitia). They study gas transport in the radial direction in the vessel according to diffusion-reaction equations solved by Bessel expansions. Such a model is

used in [147] in the context of O₂-CO₂ interaction, in [157,158,159] in the case of NO-O₂ interaction, especially when dealing with the NO scavenging mechanism in artificial RBC substitutes, see e.g.,[159].

5. Modeling of Passive and Active Regulation of Microvessels

When modeling the regulation of blood flow through a network, there are several forces acting on a vessel wall that should be considered. First, blood flow creates a pressure inside the vessel lumen that distends the vessel. Pressure external to the vessel created from the surrounding fluids, organs, and cytoskeletal structures tends to compress the vessel. The difference between the internal and external pressures is known as transmural pressure. According to the Law of Laplace [160], the circumferential tension generated within the vessel wall exactly balances the transmural pressure so that the diameter of the vessel is maintained.

The tension that is developed within the vessel wall can be divided into two main components: passive tension and active tension. Passive tension is generated by the structural components of the vessel wall such as collagen and elastin fibrils; active tension is generated in the vessel wall due to the contraction of smooth muscle cells. Vasoactive agents interact with the vascular smooth muscle (VSM) of arterioles to cause a change in muscle tone and, consequently, vessel diameter. An increase in VSM tone causes an increase in active tension and thus a constriction of the vessel; a relaxation of VSM cells causes a decrease in active tension and a dilation of the vessel. In this section, different approaches used to model blood flow regulation are reviewed, and the mechanisms to which vessels respond are summarized.

5.1. Wall mechanics models

Several studies have incorporated the passive and active components of wall tension when modeling vessel mechanics (e.g., as in Eq. 18 where T is wall tension). Gonzalez-Fernandez and Ermentrout [161] include passive and active length-tension relationships of smooth muscle in their model to predict the occurrence of vasomotion in small arteries. Passive tension is described in the model by a nonlinear function that includes terms for stiff collagen, compliant elastin fibers, and general vessel wall stiffness. Maximally active tension is represented by a modified Gaussian function. The resulting active tension is assumed to be the product of the maximally active tension and a factor between zero and one determined by intracellular calcium levels. Achakri [162] et al. propose a similar mechanism for the appearance of vasomotion that is dependent on the active behavior of vascular smooth muscle. Circumferential stress in the arterial wall is defined by the sum of passive stress (completely relaxed muscle) and active stress (contracted muscle). The nonlinear function for passive stress is based on experimental measures. The function for active stress reflects length-tension characteristics of muscle, and the level of muscle contraction is assumed to depend on the degree of activation of the contractile proteins, which depends on the concentration of calcium ions in the intracellular space. The rate of change of calcium is assumed to depend on arterial pressure and on endothelial shear stress.

Similar mechanical definitions based on length-tension characteristics described in [161,162] are used in numerous theoretical models of blood flow regulation [22,33,163,164]. In these models, the passive tension is defined as an exponential function of diameter with parameters estimated from

several experimental studies giving pressure-diameter curves for vessels with diameters ranging from 40 to 300 μm (Eq. 19). The exponential function represents the observed nonlinear behavior of tension increasing rapidly as diameter increases. A Gaussian function is used to describe the maximally active tension generated by the VSM cells in the vessel wall (Eq. 20). The activation function that determines the level of VSM tone varies between 0 and 1 and is assumed to be a sigmoidal function (Eq. 21) of a stimulus function that depends on linear combinations of various factors (see Section 5.3, Eq. 22)). In the studies that incorporate this description of wall tension the model predictions are compared with experimental data and show a good fit [22,164,165,166].

$$T_{total} = T_{pass} + AT_{act}^{max} \quad (18)$$

$$T_{pass} = C_{pass} \exp \left[C'_{pass} \left(\frac{D}{D_0} - 1 \right) \right] \quad (19)$$

$$T_{act}^{max} = C_{act} \exp \left[- \left(\frac{\frac{D}{D_0} - C'_{act}}{C''_{act}} - 1 \right)^2 \right] \quad (20)$$

$$A_{total} = \frac{1}{1 + \exp[-S_{tone}(T_{total})]} \quad (21)$$

$$S_{tone} = C_{myo}T - C_{shear}\tau_{wall} + C'_{tone} \quad (22)$$

Ursino and colleagues [50,167,168] have employed a similar modeling approach in which the inner radius of a vessel is computed from the equilibrium of forces acting on the vessel wall (Law of Laplace). Wall tension is considered the sum of elastic, smooth muscle, and viscous tensions. Regulatory mechanisms are assumed to act on the smooth muscle tension of resistance vessels (i.e. arterioles). In these models, the relationship between active tension and inner vessel radius depends on an activation factor that represents the degree of smooth muscle contraction in a given vessel. The dynamics of various regulatory mechanisms are implemented using a first-order low-pass filter characterized by a gain function and time constant. This approach developed by Ursino has been adapted in several studies, including the comprehensive model of cerebral blood flow control presented by Banaji et al. [169].

5.2. Mechanistic tube law models

In the absence of branching, a short section of vessel can be considered as a cylindrical compliant tube. One-dimensional blood flow models are obtained by averaging the incompressible Navier-Stokes equations (with constant viscosity) over a vessel cross section given some assumptions about the radial displacement and elastic material properties of the vessel wall. The following first-order, nonlinear hyperbolic system provides the one-dimensional equations for blood flow in elastic vessels:

Table 4. Models of oxygen/gas transport in blood and tissue (HL = Hill's law, MM = Michaelis-Menten, FD = finite differences, FV = finite volumes, FEM = finite elements).

Reference	Gas	Gas transport in blood	Gas transport in tissue	Blood-tissue exchange	Numerical approach	Target quantities
Moschandreou (2011) [42]	O ₂ (HL)	bi-phasic mixture with distinction in rich blood core (advection-diffusion) and plasma layer (pure diffusion) in a single arteriole	Krogh-like model with embedded mass transfer term with capillaries	continuity	FD	perivascular radial and axial O ₂ perfusion profiles, Sherwood number as a function of saturation and vessel radius
Linninger (2013) [31], Beard (2001) [170], Park (2016) [66], Fang (2008) [58], Lucker (2015) [144]	O ₂ [31], [58]: HL; [170]: Adair; HL, Clark	unsteady convection for [31], [66]: mono-phasic blood; [170]:biphasic fluid (mixture) in 3D capillary network; [144]: bi-phasic flow in a single capillary with discrete RBCs;	unsteady diffusion-reaction with [31]: first order metabolism, [170], [144]: MM with myoglobin facilitation, [66]: constant metabolic rate	[31], [66], [58]: diffusive permeation; [170], [144]: continuity	[31]: FV; [170]: FD; [58]: FEM	[31]: blood O ₂ tension in an arteriole/venule sub-unit, radial O ₂ profile; [170]: steady-state O ₂ concentration profiles as a function of O ₂ consumption, impact of myoglobin; [170]: CMRO and OEF as a function of transit time and BF; [58]:partial pressure of oxygen versus vessel diameter and O ₂ distribution in tissue; longitudinal O ₂ profiles, impact of instantaneous hematocrit fluctuations on tissue oxygenation
Safaeian (2013) [35] (2013) [178], Jespersen (2012) [171], Lemon (1987) [172], Fry (2013) [33], Goldman (2000) [173], Tsoukias (2007) [65]	[35], [171], [33]: O ₂ (HL); O ₂ (Moll); [65]: O ₂ (HL) + Hb carriers	steady convection for mono-phasic blood in [171] a single capillary (in collection of capillaries with different transit times) or [33], [173] vessel/capillary network, bi-phasic mixture in [35], [65] anatomical network or [172] single capillary	[35], [33]: steady diffusion-reaction in 3D volume; [171], [172]: given constant O ₂ pressure in tissue; [173], [65]: steady diffusion-reaction with myoglobin facilitation	[35]: pointwise sources; [171], [172], [65]: first order exchange with permeation; [33]: pointwise sources; [173]: hematocrit dependent permeation	[178], [160]: Green's function method, [172]: FD + FEM; [173], [65]: FD	tissue O ₂ pressure distribution for different CMRO and perfusion levels, OEF as a function of BF (comparison with Buxton model); [171]: net O ₂ extraction as a function of transit time, tissue O ₂ concentration and capillary arrangement; [172]: O ₂ profiles in radial and axial directions as a function of chemical equilibrium parameters; [33]: O ₂ contour curves in tissue slices for different CMRO; [173]: study of geometric factors (shunts, tortuosity) in O ₂ levels in tissue and axial O ₂ profiles in capillaries; [65]: PO in the capillaries and O ₂ in tissue as a function of the Hb substitute

Eggleton (2000) [143]	O ₂	unsteady diffusion in single erythrocytes and plasma in a capillary vessel	unsteady diffusion-convection in annular muscular region	FEMs in a frame moving with RBC velocity		radial O ₂ profile, local mass transfer coefficient for 1s simulated time, MTC
Tsoukias (2003) [174], Chen (2007) [138]	[174]: NO, O ₂ + NO	steady diffusion-convection-reaction for [174] capillary with discrete parachute-shaped RBCs, [138] straight arteriole and venule pair;	[174]: steady diffusion-convection-reaction for 2D tissue and interstitium; [138]: diffusion-convection porous medium perfused by capillaries	[174]: continuity + (flux continuity with sources); [138]: first order reaction	[174]: FEM + moving frame for RBCs; [138]: semi-analytic	[174]: NO contour curves, comparison between discrete cell and continuum model, estimation of intravascular MTC; [138]: NO profiles, effect of capillary-perfused tissue
Vazquez (2008) [56], Barrett (2013) [57]	O ₂ (HL)	unsteady balance for monophasic blood in [56] in capillary compartment, [57] arteries, capillaries, veins	unsteady compartmental reaction	permeation	ODE solver	lumped tissue compartment; tissue and vascular O ₂ as a function of time for different permeability increase; [57]: sensitivity analysis on permeation parameter
Reichold (2009) [18]	generic solute	unsteady graph-based 1D advection for monophasic fluid with upscaling procedure	unsteady diffusion-reaction with upscaling	permeation	FV	solute levels in tissue

$$\frac{\partial A}{\partial t} + \frac{\partial q}{\partial x} = 0 \quad (23)$$

$$\frac{\partial q}{\partial t} + \frac{\partial}{\partial x} \left(\alpha \frac{q^2}{A} \right) + \frac{A}{\rho} \frac{\partial p}{\partial x} = -f \quad (24)$$

where x is the axial coordinate along the longitudinal axis of the vessel, t is time, $A(x,t)$ is the cross-sectional area of the vessel, $q(x,t)$ is blood flow, $p(x,t)$ is the average internal pressure over a cross section, $f(x,t)$ is the friction force per unit length of the tube, ρ is the fluid density, and α is a coefficient that depends on the velocity profile assumed in the system.

A complete derivation of these equations is provided in [80]. A tube law is implemented to close the system, where the transmural pressure (i.e., the difference between the internal pressure $p(x,t)$ and external pressure $p_e(x,t)$) is a function of cross-sectional area $A(x,t)$ of the vessel and other parameters related to the geometric and mechanical properties of the system such the elasticity and stress-strain response curves for a vessel. Multiple different functions can be used to express this pressure-area relationship. Appropriate choices for such functions and parameters for both arteries and veins are described by Muller et al. They implement this tube law modeling approach when studying cerebral venous flow [20] and when developing a global multiscale model for the human circulation [54].

Similarly, fluid dynamic equations are derived from the continuity equation and momentum equation by Olufsen et al. [25]. In such models, the pressure-area relationship is shown to depend on Young's modulus (E) in the circumferential direction. Young's modulus is assumed to vary based on vessel type to reflect the elastin content of the vessel wall at different points along the arterial tree. For example, since small arteries are stiffer, E is chosen to be a function of vessel radius based on compliance estimates. In this way, the structural components of vessels are incorporated correctly into theoretical models.

5.3. Factors eliciting a vasodilatory response in resistance vessels

The models described in Sections 5.1 and 5.2 describe changes in vessel diameter due to various stimuli. Depending on the tissue and the metabolic conditions, vessels are known to respond to a great multitude of factors, including: pressure (myogenic response), shear stress, ATP concentration (conducted metabolic response), local metabolic factors, carbon dioxide concentration, hormones, neurological stimuli, and tubuloglomerular feedback. For example, in exercising muscle, metabolites from contracting muscle can cause direct vasodilation of resistance arterioles or indirect inhibition of noradrenaline release from nerves to prevent vasoconstriction [175]. Vasodilatory factors also affect vessels to very different extents depending on the size of the vessel. For example, sympathetic innervation is more pronounced in small vessels while the endothelium of large resistance vessels releases dilatory factors like nitric oxide at a much higher rate than small vessels [176]. Responsiveness to pressure (myogenic responsiveness) is expressed more distinctly in smaller vessels than larger vessels in some cases [176]. Despite differences in their reactivity, it has been shown that large and small vessels react in a coordinated manner, which is critical for an appropriate vasodilatory response. Network geometry also plays a role vasoactive responses. For example, the

anatomical relationship between pre- and post-capillary vessels allows for the diffusive exchange of substances between these vessels, providing important information about distal tissue regions to proximal vessels in the network [177].

6. Focus: Modeling of the Retinal Circulation

Various modeling techniques described in this article have been applied to understanding the geometry, mechanics and hemodynamics of the retinal microcirculation under both healthy and disease conditions. In this section, the various modeling techniques and methods used to study the retinal circulation are reviewed.

6.1. Anatomic summary

The retina is the sensitive tissue lining the back of the eye. It collects the visual signal and sends it to the brain in the form of a neural signal. These tasks imply high oxygen demands. The retina receives oxygen from two distinct vascular systems [178]: the retinal blood vessels and the choroidal blood vessels (see 3). The first system specifically provides nourishment to the innermost retinal layers, while the choroid choriocapillaris provide nourishment via diffusion to the outermost retinal layers, which are normally avascular. Oxygenated blood is supplied to the retina by the central retinal artery (CRA) which, at the entrance of the optic nerve head, is approximately 170 μm in diameter. The CRA branches into the superior and inferior papillary arteries, which in turn divide again, with each branch supplying roughly a quadrant of the retina. The major branching arteries are approximately 120 μm in diameter. In the posterior retina, the fine arterioles that arise by side-arm branching leave the main arteries and enter the inner plexiform and ganglion cell layers. Only capillaries are found as deep as the inner nuclear layer. The venous system of the retina usually mirrors the arteriolar circulation. De-oxygenated blood is drained from the capillaries into successively larger veins that eventually converge into the central retinal vein (CRV). At the entrance of the optic nerve head, the CRV is approximately 220 μm in diameter.

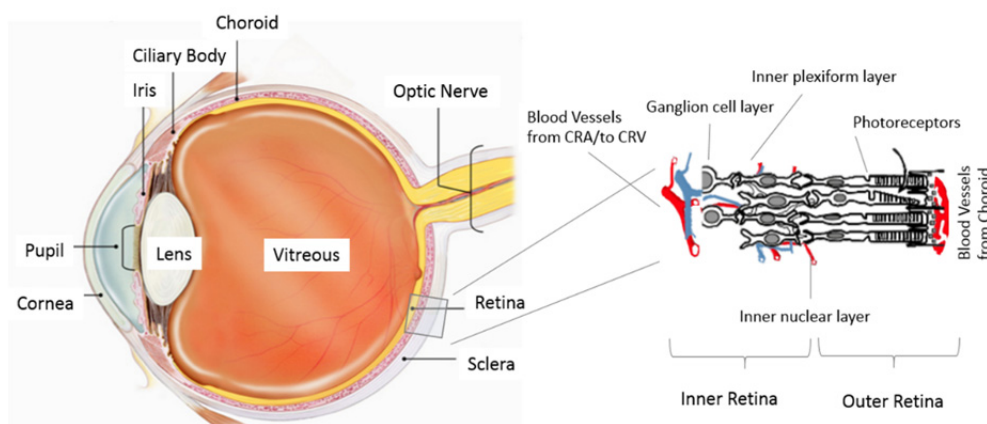


Figure 3. Left: diagram of the lateral view of the eye; right: schematic section along retinal thickness with the blood supply system and the indication of the retinal layers mentioned in the text.

6.2. Geometric models of blood flow in the retinal circulation

Takahashi et al. [23,61] developed a model of the microvasculature of the human retina using a fractal dichotomous branching structure. The model included arterioles stemming from the CRA, capillaries and venules converging into the CRV. Symmetric as well non-symmetric networks were considered. The model was used to quantify parameters such as blood pressure, blood flow, blood velocity, shear rate, and shear stress as a function of vessel diameter in the retinal microcirculation. Ganesan et al. [27] introduced a more realistic network model of the retina using confocal microscopy images from a mouse retina to develop a complex network of microvessels that are distributed non-uniformly into multiple distinct retinal layers at varying depths. In the model, capillaries were represented as a circular mesh consisting of concentric rings along which several uniformly distributed nodes represent capillary vessels. The study defined a series of rules that explains the process of connecting the capillary network to arterial and venous networks to provide a complete and comprehensive vascular network of the retinal circulation. The model predicted the non-uniform repartition of blood hematocrit in the retina. In [179], Aletti et al. studied fluid-structure interactions in a 3D network representing the inferior temporal arteriole tree in the human retina. Typical diameters of the network were between 70 μm and 160 μm . They proposed a simplified model that could be used to solve the fluid problem on a fixed domain, where Robin-like boundary conditions represented the effect of the solid wall. In [180], Causin et al. adapted the geometry proposed by Takahashi in [61] to describe the retinal network. Blood flow and pressure drop in each vessel were related through a generalized Ohm's law featuring a conductivity parameter, function of the area and shape of the vascular cross section. The model was used to study the response of the network to different interstitial and outlet pressures (or intraocular pressure, IOP). Phenomena of flow plateau, choking and flow diversion from one branch of the system to the other were predicted.

6.3. Retinal blood flow regulation models

Blood flow is regulated in the retina according to mechanistic responses to intraluminal pressure (myogenic response), shear stress, metabolite concentrations, and neural stimuli. Arciero et al. [22] developed a model that assessed the relative contributions of myogenic, shear, conducted metabolic, and carbon dioxide responses to blood flow in the retina. The model predicted that the metabolic responses were most significant in obtaining autoregulation of flow. This model has served as a foundation upon which more recent models have been developed to combine a mechanistic description of blood flow autoregulation in the retinal microcirculation with the mechanistic models described in Section 3. Arciero et al. [166], Carichino et al. [181] and Cassani et al. [182] have implemented Krogh-type models within a compartmental representation of the retinal microcirculation. These models yield predictions of blood flow that are consistent with experimental measures but do not capture the spatial variation of oxygen levels in retinal tissue. In [29], Causin et al. coupled a wall mechanics model with a model for oxygen transport in the retina and quantified the effects of blood pressure, blood rheology, arterial permeability to oxygen, and tissue oxygen demand on the distribution of oxygen in retinal blood vessels and tissue.

6.4. Models of gas transport in the retinal tissue

Several models have been developed to estimate oxygen profiles in the avascular region of the retina (outer retina). Cringle and colleagues studied (see, e.g., [183,184]) oxygen delivery to the outer retina by 1D reaction-diffusion equations with constant or linear oxygen consumption in the region corresponding to photoreceptor mitochondria. The source of oxygen from choroid (not represented) was modeled as a boundary condition. The inclusion of the inner retinal layers along with the embedded blood sources in the inner retinal layer was proposed by Roos [185]. Oxygen sources were embedded in the inner retina via a prescribed flux term depending on blood convection. The effect of arterial occlusion was investigated, blocking the supply of blood from the inner retina. The results suggested that extreme hyperoxia would be needed to make the choroid capable of supplying oxygen to the entire retina by itself.

One of the difficulties in modeling gas transport in the retina is that important parameters such as the average thickness of the retina, the choroidal tension and the structure of the inner retinal vascularization present relevant intra and inter-species differences. These model parameters are often fit to experimental data. For example, in [186] it was found by linear regression that the most metabolically active region extended from about 75% to 85% of the retinal depth from the vitreous.

Table 5. Summary of blood flow regulation mechanisms in mathematical models of the microcirculation.

Regulatory mechanism	Model implementation	Effect on vessel diameter
myogenic response	[166], [165], [163], [22], [187], [33], [188], [189]	vasoconstriction
shear-dependent response	[187], [33], [52], [166], [22], [163], [165]	vasodilation
local metabolic response	[187], [190]	vasodilation
conducted metabolic response	[166], [22], [163], [33]	vasodilation
CO ₂ response	[52], [166]	vasodilation
neural stimuli	[191], [50], [52]	Vasoconstriction or vasodilation

6.5. Mechanistic models in retinal circulation

The vasculature system of the retina is subjected to multiple mechanical forces. Intraocular pressure (IOP) from the anterior chamber of the eye, cerebral spinal fluid (CSF) pressure from the brain and tensions that come from the sclera exert significant biomechanical actions. The role of these actions is especially relevant near the entrance of the optic nerve head (ONH), where the nerve bundles pass through a sieve-like portion of sclera called lamina cribrosa (LC). The LC is also pierced by the CRA and CRV. Several mathematical models have described the mechanical response of the optic nerve head to variations in IOP, scleral tension and CSF pressure and its correlation to pathological conditions, in particular open angle glaucoma (see, e.g., [192–195]). In [196], Harris et al. analyzed the role of mathematical models in assessing how hemodynamic alterations may contribute to open angle glaucoma pathophysiology. A recent model by Guidoboni et al. [197] was

used to predict the effects of IOP, CSF pressure, and scleral tension on the deformation of the LC and the resulting effect on the flow of blood through the CRA and CRV. This information was incorporated into a more comprehensive model of the retina that accounts for the compression of the CRA/CRV by the lamina as well as blood flow regulatory mechanisms while IOP and mean arterial pressure (MAP) are varied [198]. The model represents veins as Starling resistors and accounts for venous compressibility. The model predicts that an increase in IOP or decrease in MAP do not have the same effect on ocular perfusion pressure due to the built-in compensatory mechanism in the veins to increase blood pressure in the retinal vasculature. In [199], Causin et al. demonstrated the relationship between stress state in the LC and blood perfusion using a poroelastic material model where blood vessels are viewed as pores in a solid elastic matrix. The model was used to investigate the influence on the distributions of stress, blood volume fraction (or vascular porosity) and blood velocity within the lamina cribrosa due to different levels of IOP and different mechanical constraints at the boundary of the lamina. The model simulations suggest that the degree of fixity of the boundary constraint strongly influences the lamina's response to IOP elevation.

7. Conclusions and Perspectives

It was in 1661 that the physiologist M. Malpighi published the treatise "*De pulmonibus observationes anatomicae*" where he exposed the results of his observations of frog pulmonary alveoli obtained with a single lens microscope. His studies revealed for the first time the existence of a very fine network of vessels connecting arteries and veins. The importance of this discovery, and all the successive studies opened by it, is major. The microcirculation plays a fundamental role in the homeostasis of the body. Microcirculatory disorders are major contributors to morbidity and mortality. In the past few decades, much progress has been made in the mathematical and computational modeling of these complex systems. Their hierarchical structure includes at least three modeling scales, ranging from the cellular level to the vessel network level. There is a strong coupling of microvessels with the surrounding parenchymal tissue and cells. Feed-forward and feedback interactions have been envisaged [200]. The scenario is thus very complex. On the computational side, the applicability of high performance computing techniques favors large scale simulations, based on 3D anatomic models. This will be a steadily growing trend in future models. However, important gaps must still be filled. For example, to what extent can detailed single vessel simulations be enlarged to a network of thousands of vessels? Is the information from a single RBC tractable (and meaningful) to a much larger scale? What are appropriate upscaling techniques to transfer information between scales? These are only a few aspects that must be considered to advance in this field. Finally, we note that in this study we did not review the fundamental topic of drug delivery. The microcirculation is the ultimate site of exchange of substances/molecules and also functions as an important route for clearance. The delivery of drugs to certain organs can be difficult, such as in the brain due to the tight blood-barrier. Studies and numerical simulations of drug delivery rely on the precise knowledge of microcirculatory mechanisms. A correct representation of these latter is a fundamental background to obtain meaningful results.

Conflict of Interest

The authors declare no conflict of interest in this paper.

References

1. Tuma R, Duran WN, Ley K (2008) Microcirculation. 2Eds., Elsevier.
2. Gutterman DD, Chabowski DS, Kadlec AO, et al. (2016) The human microcirculation: regulation of flow and beyond. *Circ Res* 118: 157–172.
3. Mortillaro N (1983) The physiology and pharmacology of the microcirculation. Elsevier.
4. Dalkara T (2015) Cerebral Microcirculation: An Introduction, In: Lanzer P, Editor, Springer Berlin Heidelberg, 655–680.
5. Navar LG, Arendshorst WJ, Pallone TL, et al. (2011) The renal microcirculation. *Compr Physiol* 9: 550–683.
6. Kviety PR (2010) The gastrointestinal circulation. Morgan & Claypool Life Sciences.
7. Ivanov KP (2013) Circulation in the lungs and microcirculation in the alveoli. *Respir Physiol Neurobiol* 187: 26–30.
8. Murray A, Dinsdale G (2016) Imaging the microcirculation. *Microcirculation* 23: 335–336.
9. Leahy M (2012) Microcirculation Imaging. Wiley-Blackwell.
10. Eriksson S, Nilsson J, Stureson C (2014) Non-invasive imaging of microcirculation: a technology review. *Med Devices* 7: 445–452.
11. Secomb TW, Beard DA, Frisbee JC, et al. (2008) The role of theoretical modeling in microcirculation research. *Microcirculation* 15: 693–698.
12. Lee J, Smith NP (2008) Theoretical modeling in hemodynamics of microcirculation. *Microcirculation* 15: 699–714.
13. Popel AS, Johnson PC (2005) Microcirculation and hemorheology. *Annu Rev Fluid Mech* 37: 43–69.
14. Gompper G, Fedosov DA (2016) Modeling microcirculatory blood flow: current state and future perspectives. *Wiley Interdiscip Rev Syst Biol Med* 8: 157–168.
15. Secomb TW (2017) Blood flow in the microcirculation. *Annu Rev Fluid Mech* 49: 443–461.
16. Liu D, Wood NB, Witt N, et al. (2009) Computational analysis of oxygen transport in the retinal arterial network. *Curr Eye Res* 34: 945–956.
17. Gould IG, Linninger AA (2015) Hematocrit distribution and tissue oxygenation in large microcirculatory networks. *Microcirculation* 22: 1–18.
18. Reichold J, Stampanoni M, Keller AL, et al. (2009) Vascular graph model to simulate the cerebral blood flow in realistic vascular networks. *J Cereb Blood Flow Metab* 29: 1429–1443.
19. Guibert R, Fonta C, Plouraboué F (2010) A new approach to model confined suspensions flows in complex networks: application to blood flow. *Transport Porous Med* 83: 171–194.
20. Muller LO, Toro EF (2014) Enhanced global mathematical model for studying cerebral venous blood flow. *J Biomech* 47: 3361–3372.
21. Ursino M, Lodi CA (1997) A simple mathematical model of the interaction between intracranial pressure and cerebral hemodynamics. *J Appl Physiol* 82: 1256–1269.
22. Arciero JC, Carlson BE, Secomb TW (2008) Theoretical model of metabolic blood flow regulation: roles of ATP release by red blood cells and conducted responses. *Am J Physiol Heart Circ Physiol* 295: H1562–H1571.
23. Takahashi T, Nagaoka T, Yanagida H, et al. (2009) A mathematical model for the distribution of hemodynamic parameters in the human retinal microvascular network. *J Biorheol* 23: 77–86.
24. Gabryś E, Rybaczuk M, Kędzia A (2005) Fractal models of circulatory system. Symmetrical

- and asymmetrical approach comparison. *Chaos, Solitons & Fractals* 24: 707–715.
25. Olufsen MS, Peskin CS, Kim WY, et al. (2000) Numerical simulation and experimental validation of blood flow in arteries with structured-tree outflow conditions. *Ann Biomed Eng* 28: 1281–1299.
 26. David T, Alzaidi S, Farr H (2009) Coupled autoregulation models in the cerebro-vasculature. *J Eng Math* 64: 403–415.
 27. Ganesan P, He S, Xu H (2011) Development of an image-based model for capillary vasculature of retina. *Comput Meth Prog Bio* 102: 35–46.
 28. Schröder S, Schmid-Schönbein GW, Schmid-Schönbein H, et al. (1990) A method for recording the network topology of human retinal vessels. *Klin Monbl Augenheilkd* 197: 33–39.
 29. Causin P, Guidoboni G, Malgaroli F, et al. (2016) Blood flow mechanics and oxygen transport and delivery in the retinal microcirculation: multiscale mathematical modeling and numerical simulation. *Biomech Model Mechanobiol* 15: 525–542.
 30. Pan Q, Wang R, Reglin B, et al. (2014) A one-dimensional mathematical model for studying the pulsatile flow in microvascular networks. *J Biomech Eng* 136: 011009.
 31. Linninger AA, Gould IG, Marinnan T, et al. (2013) Cerebral microcirculation and oxygen tension in the human secondary cortex. *Ann Biomed Eng* 41: 2264–2284.
 32. Gould I, Tsai P, Kleinfeld D, et al. (2017) The capillary bed offers the largest hemodynamic resistance to the cortical blood supply. *J Cereb Blood Flow Metab* 37: 52–68.
 33. Fry BC, Roy TK, Secomb TW (2013) Capillary recruitment in a theoretical model for blood flow regulation in heterogeneous microvessel networks. *Physiol Rep* 1: e00050.
 34. Su SW, Catherall M, Payne S (2012) The influence of network structure on the transport of blood in the human cerebral microvasculature. *Microcirculation* 19: 175–187.
 35. Safaeian N, David T (2013) A computational model of oxygen transport in the cerebrocapillary levels for normal and pathologic brain function. *J Cereb Blood Flow Metab* 33: 1633–1641.
 36. Soltani M, Chen P (2013) Numerical modeling of interstitial fluid flow coupled with blood flow through a remodeled solid tumor microvascular network. *PLoS One* 8: e67025.
 37. Sefidgar M, Soltania M, Raahemifarc K, et al. (2015) Numerical modeling of drug delivery in a dynamic solid tumor microvasculature. *Microvasc Res* 99: 43–56.
 38. Levine H, Pamuk S, Sleeman B, et al. (2002) Mathematical modeling of capillary formation and development in tumor angiogenesis: penetration into the stroma. *Bull Math Biol* 63: 801–863.
 39. Rieger H, Welter M (2015) Integrative models of vascular remodeling during tumor growth. *Wiley Interdiscip Rev Syst Biol Med* 7: 113–129.
 40. Erbertseder K, Reichold J, Flemisch B, et al. (2012) A coupled discrete/continuum model for describing cancer-therapeutic transport in the lung. *PLoS One* 7: e31966.
 41. Dash RK, Bassingthwaight JB (2006) Simultaneous blood-tissue exchange of oxygen, carbon dioxide, bicarbonate, and hydrogen ion. *Ann Biomed Eng* 34: 1129–1148.
 42. Moschandreou TE, Ellis CG, Goldman D (2011) Influence of tissue metabolism and capillary oxygen supply on arteriolar oxygen transport: a computational model. *Math Biosci* 232: 1–10.
 43. Welter M, Rieger H (2016) Computer simulations of the tumor vasculature: applications to interstitial fluid flow, drug delivery, and Oxygen supply. *Adv Exp Med Biol* 936: 31–72.
 44. Preziosi L, Tosin A (2009) Multiphase and multiscale trends in cancer modelling. *Math Model Nat Phenom* 4: 1–11.

45. Cornelis F, Sautd O, Cumsillea P, et al. (2013) In vivo mathematical modeling of tumor growth from imaging data: Soon to come in the future? *Diagn Interv Imaging* 94: 593–600.
46. Wu J, Xu S, Long Q, et al. (2008) Coupled modeling of blood perfusion in intravascular, interstitial spaces in tumor microvasculature. *J Biomech* 41: 996–1004.
47. Ye GF, Moore TW, Jaron D (1993) Contributions of oxygen dissociation and convection to the behavior of a compartmental oxygen transport model. *Microvasc Res* 46: 1–18.
48. Piechnik SK, Chiarelli PA, Jezzard P (2008) Modelling vascular reactivity to investigate the basis of the relationship between cerebral blood volume and flow under CO₂ manipulation. *Neuroimage* 39: 107–118.
49. Fantini S (2014) Dynamic model for the tissue concentration and oxygen saturation of hemoglobin in relation to blood volume, flow velocity, and oxygen consumption: Implications for functional neuroimaging and coherent hemodynamics spectroscopy (CHS). *Neuroimage* 85: 202–221.
50. Ursino M, Lodi CA (1998) Interaction among autoregulation, CO₂ reactivity, and intracranial pressure: a mathematical model. *Am J Physiol* 274: H1715–H1728.
51. Spronck B, Martens EG, Gommer ED, et al. (2012) A lumped parameter model of cerebral blood flow control combining cerebral autoregulation and neurovascular coupling. *Am J Physiol Heart Circ Physiol* 303: H1143–H1153.
52. Payne S (2006) A model of the interaction between autoregulation and neural activation in the brain. *Math Biosci* 204: 260–281.
53. Diamond SG, Perdue KL, Boas DA (2009) A cerebrovascular response model for functional neuroimaging including dynamic cerebral autoregulation. *Math Biosci* 220: 102–117.
54. Muller LO, Toro EF (2014) A global multiscale mathematical model for the human circulation with emphasis on the venous system. *Int J Numer Method Biomed Eng* 30: 681–725.
55. Gutierrez G (2004) A mathematical model of tissue-blood carbon dioxide exchange during hypoxia. *Am J Respir Crit Care Med* 169: 525–533.
56. Vazquez AL, Masamoto K, Kim SG (2008) Dynamics of oxygen delivery and consumption during evoked neural stimulation using a compartment model and CBF and tissue P(O₂) measurements. *Neuroimage* 42: 49–59.
57. Barrett MJ, Suresh V (2013) Extra permeability is required to model dynamic oxygen measurements: evidence for functional recruitment? *J Cereb Blood Flow Metab* 33: 1402–1411.
58. Fang Q, Sakadžić S, Ruvinskaya L, et al. (2008) Oxygen advection and diffusion in a three dimensional vascular anatomical network. *Opt Express* 16: 17530–17541.
59. Lorthois S, Cassot F, Lauwers F (2011) Simulation study of brain blood flow regulation by intra-cortical arterioles in an anatomically accurate large human vascular network: Part I: methodology and baseline flow. *Neuroimage* 54: 1031–1042.
60. Boas DA, Jones SR, Devor A, et al. (2008) A vascular anatomical network model of the spatio-temporal response to brain activation. *Neuroimage* 40: 1116–1129.
61. Takahashi T (2014) Microcirculation in fractal branching networks. Springer Japan.
62. Ganesan P, He S, Xu H (2010) Analysis of retinal circulation using an image-based network model of retinal vasculature. *Microvasc Res* 80: 99–109.
63. El-Bouri WK, Payne SJ (2015) Multi-scale homogenization of blood flow in 3-dimensional human cerebral microvascular networks. *J Theor Biol* 380: 40–47.

64. Gagnon L, Sakadžić S, Lesage F, et al. (2015) Multimodal reconstruction of microvascular-flow distributions using combined two-photon microscopy and Doppler optical coherence tomography. *Neurophotonics* 2: 015008–015008.
65. Tsoukias NM, Goldman D, Vadapalli A, et al. (2007) A computational model of oxygen delivery by hemoglobin-based oxygen carriers in three-dimensional microvascular networks. *J Theor Biol* 248: 657–674.
66. Park CS, Payne SJ (2016) Modelling the effects of cerebral microvasculature morphology on oxygen transport. *Med Eng Phys* 38: 41–47.
67. Gorodnova NO, Kolobov AV, Mynbaev OA, et al. (2016) Mathematical modeling of blood flow alteration in microcirculatory network due to angiogenesis. *Lobachevskii J Math* 37: 541–549.
68. Cristini V, Kassab GS (2005) Computer modeling of red blood cell rheology in the microcirculation: a brief overview. *Ann Biomed Eng* 33: 1724–1727.
69. Sriram K, Intaglietta M, Tartakovsky DM (2014) Non-Newtonian flow of blood in arterioles: consequences for wall shear stress measurements. *Microcirculation* 21: 628–639.
70. Kim S, Ong PK, Yalcin O, et al. (2009) The cell-free layer in microvascular blood flow. *Biorheology* 46: 181–189.
71. Pries AR, Secomb TW (2003) Rheology of the microcirculation. *Clin Hemorheol Microcirc* 29: 143–148.
72. Ganesan P, He S, Xu H (2011) Modelling of pulsatile blood flow in arterial trees of retinal vasculature. *Med Eng Phys* 33: 810–823.
73. Secomb TW, Pries AR (2013) Blood viscosity in microvessels: experiment and theory. *C R Phys* 14: 470–478.
74. Pries AR, Secomb TW (2005) Microvascular blood viscosity in vivo and the endothelial surface layer. *Am J Physiol Heart Circ Physiol* 289: H2657–H2664.
75. Lipowsky HH, Usami S, Chien S (1980) In vivo measurements of “apparent viscosity” and microvessel hematocrit in the mesentery of the cat. *Microvasc Res* 19: 297–319.
76. Haynes RH (1960) Physical basis of the dependence of blood viscosity on tube radius. *Am J Physiol* 198: 1193–1200.
77. Neofytou P (2004) Comparison of blood rheological models for physiological flow simulation. *Biorheology* 41: 693–714.
78. Hellums JD, Nair PK, Huang NS, et al. (1996) Simulation of intraluminal gas transport processes in the microcirculation. *Ann Biomed Eng* 24: 1–24.
79. Hellums JD (1977) The resistance to oxygen transport in the capillaries relative to that in the surrounding tissue. *Microvasc Res* 13: 131–136.
80. Formaggia L, Quarteroni A (2009) Cardiovascular mathematics: modeling and simulation of the circulatory system. Milan: Springer-Verlag.
81. Pries AR, Ley K, Claassen M, et al. (1989) Red cell distribution at microvascular bifurcations. *Microvasc Res* 38: 81–101.
82. Canic S, Kim EH (2003) Mathematical analysis of the quasilinear effects in a hyperbolic model blood flow through compliant axi-symmetric vessels. *Math Method Appl Sci* 26: 1161–1186.
83. Gagnon L, Smith AF, Boas DA, et al. (2016) Modeling of cerebral oxygen transport based on in vivo microscopic imaging of microvascular network structure, blood flow, and oxygenation. *Front Comput Neurosci* 1.
84. Nair PK, Huang NS, Hellums JD, et al. (1990) A simple model for prediction of oxygen

- transport rates by flowing blood in large capillaries. *Microvasc Res* 39: 203–211.
85. Pandey HM, Negi DS, Bisht MS (2011) The study of mathematical modelling of human blood circulatory system. *Int J Math Scis Appl* 1: 425–434.
 86. Sharan M, Popel AS (2001) A two-phase model for flow of blood in narrow tubes with increased effective viscosity near the wall. *Biorheology* 38: 415–428.
 87. Namgung B, Ju M, Cabrales P, et al. (2013) Two-phase model for prediction of cell-free layer width in blood flow. *Microvasc Res* 85: 68–76.
 88. Chebbi R (2015) Dynamics of blood flow: modeling of the Fåhræus-Lindqvist effect. *J Biol Phys* 41: 313–326.
 89. Verma SR, Srivastava A (2014) Analytical study of a two-phase model for steady flow of blood in a circular tube. *IJERA* 12: 1–10.
 90. Das B, Johnson PC, Popel AS (1998) Effect of nonaxisymmetric hematocrit distribution on non-Newtonian blood flow in small tubes. *Biorheology* 35: 69–87.
 91. Gupta BB, Nigam KM, Jaffrin MY (1982) A three-layer semi-empirical model for flow of blood and other particular suspensions through narrow tubes. *J Biomech Eng* 104: 129.
 92. Walburn FJ, Schneck DJ (1976) A constitutive equation for whole human blood. *Biorheology* 13: 201–210.
 93. Zaman A, Ali N, Sajid M, et al. (2016) Numerical and analytical study of two-layered unsteady blood flow through catheterized artery. *PLoS One* 11: e0161377.
 94. Secomb TW, Pries AR (2011) The microcirculation: physiology at the mesoscale. *J Physiol* 589: 1047–1052.
 95. AlMomani TD, Vigmostad SC, Chivukula VK, et al. (2012) Red blood cell flow in the cardiovascular system: a fluid dynamics perspective. *Crit Rev Biomed Eng* 40: 427–440.
 96. Chung B, Johnson PC, Popel AS (2007) Application of Chimera grid to modelling cell motion and aggregation in a narrow tube. *Int J Numer Meth Fluids* 53: 105–128.
 97. Ye T, Phan-Thien N, Lim CT (2016) Particle-based simulations of red blood cells—A review. *J Biomech* 49: 2255–2266.
 98. Tsubota K, Wada S (2010) Effect of the natural state of an elastic cellular membrane on tank-treading and tumbling motions of a single red blood cell. *Phys Rev E Stat Nonlin Soft Matter Phys* 81: 011910.
 99. Nakamura M, Bessho S, Wada S (2013) Spring-network-based model of a red blood cell for simulating mesoscopic blood flow. *Int J Numer Method Biomed Eng* 29: 114–128.
 100. Hariprasad DS, Secomb TW (2014) Two-dimensional simulation of red blood cell motion near a wall under a lateral force. *Phys Rev E Stat Nonlin Soft Matter Phys* 90: 053014.
 101. Pozrikidis C (2003) Numerical simulation of the flow-induced deformation of red blood cells. *Ann Biomed Eng* 31: 1194–1205.
 102. Gounley J, Peng Y (2015) Computational modeling of membrane viscosity of red blood cells. *Commun Comput Phys* 17: 1073–1087.
 103. Eggleton CD, Popel AS (1998) Large deformation of red blood cell ghosts in a simple shear flow. *Phys Fluids* 10: 1834–1845.
 104. Bagchi P (2007) Mesoscale simulation of blood flow in small vessels. *Biophys J* 92: 1858–1877.
 105. Sun C, Munn LL (2005) Particulate nature of blood determines macroscopic rheology: A 2-D lattice Boltzmann analysis. *Biophys J* 88: 1635–1645.

106. Li X, Sarkar K (2008) Front tracking simulation of deformation and buckling instability of a liquid capsule enclosed by an elastic membrane. 227: 4998–5018.
107. Pan TW, Wang T (2009) Dynamical simulation of red blood cell rheology in microvessels. *Int J Numer Anal Mod* 6: 455–473.
108. Bessonov N, Crauste F, Fischer S, et al. (2011) Application of hybrid models to blood cell production in the bone marrow. *Math Model of Nat Phenom* 6: 2–12.
109. Volpert V, Bessonov N, Sequeira A, et al. (2015) Methods of blood flow modelling. *Math Model Nat Phenom* 11: 1–25.
110. Munn LL, Dupin MM (2008) Blood cell interactions and segregation in flow. *Ann Biomed Eng* 36: 534–544.
111. Volpert V, Pujo-Menjouet L (2016) Blood cell dynamics: half of a century of modelling. *Math Model Nat Phenom* 11: 92–115.
112. Imai Y, Omori T, Shimogonya Y, et al. (2016) Numerical methods for simulating blood flow at macro, micro, and multi scales. *J Biomech* 49: 2221–2228.
113. Liu Y, Liu WK (2006) Rheology of red blood cell aggregation by computer simulation. *J Comput Phys* 220: 139–154.
114. Liu Y, Zhang L, Wang X, et al. (2004) Coupling of Navier-Stokes equations with protein molecular dynamics and its application to hemodynamics. *Int J Numer Meth Fluids* 46: 1237–1252.
115. Bagchi P, Johnson PC, Popel AS (2005) Computational fluid dynamic simulation of aggregation of deformable cells in a shear flow. *J Biomech Eng* 127: 1070–1080.
116. Le DV, White J, Peraire J, et al. (2009) An implicit immersed boundary method for three-dimensional fluid-membrane interactions. *J Comput Phys* 228: 8427–8445.
117. Wu T, Feng JJ (2013) Simulation of malaria-infected red blood cells in microfluidic channels: Passage and blockage. *Biomicrofluidics* 7: 44115.
118. Ju M, Ye SS, Namgung B, et al. (2015) A review of numerical methods for red blood cell flow simulation. *Comput Methods Biomech Biomed Engin* 18: 130–140.
119. Shaw S, Ganguly S, Sibanda P, et al. (2014) Dispersion characteristics of blood during nanoparticle assisted drug delivery process through a permeable microvessel. *Microvasc Res* 92: 25–33.
120. Shipley RJ, Chapman SJ (2010) Multiscale modelling of fluid and drug transport in vascular tumours. *Bull Math Biol* 72: 1464–1491.
121. Pittman RN (2011) Regulation of Tissue Oxygenation. Morgan & Claypool Life Sciences.
122. Popel AS (1989) Theory of oxygen transport to tissue. *Crit Rev Biomed Eng* 17: 257–321.
123. Goldman D (2008) Theoretical models of microvascular oxygen transport to tissue. *Microcirculation* 15: 795–811.
124. Krogh A (1919) The supply of oxygen to the tissues and the regulation of the capillary circulation. *J Physiol* 52: 457–474.
125. Buxton RB, Frank LR (1997) A model for the coupling between cerebral blood flow and oxygen metabolism during neural stimulation. *J Cereb Blood Flow Metab* 17: 64–72.
126. Buxton RB, Uludag K, Dubowitz DJ, et al. (2004) Modeling the hemodynamic response to brain activation. *Neuroimage* 23 (Suppl 1): S220–S233.
127. Secomb TW (2015) Krogh-cylinder and infinite-domain models for washout of an inert diffusible solute from tissue. *Microcirculation* 22: 91–98.

128. Schumacker PT, Samsel RW (1989) Analysis of oxygen delivery and uptake relationships in the Krogh tissue model. *J Appl Physiol* 67: 1234–1244.
129. Lagerlund TD, Low PA (1991) Axial diffusion and Michaelis-Menten kinetics in oxygen delivery in rat peripheral nerve. *Am J Physiol* 260: R430–R440.
130. Piiper J, Scheid P (1991) Diffusion limitation of O₂ supply to tissue in homogeneous and heterogeneous models. *Respir Physiol* 85: 127–136.
131. Whiteley JP, Gavaghan DJ, Hahn CE (2003) Mathematical modelling of pulmonary gas transport. *J Math Biol* 47: 79–99.
132. McGuire BJ, Secomb TW (2001) A theoretical model for oxygen transport in skeletal muscle under conditions of high oxygen demand. *J Appl Physiol* 91: 2255–2265.
133. McGuire BJ, Secomb TW (2003) Estimation of capillary density in human skeletal muscle based on maximal oxygen consumption rates. *Am J Physiol Heart Circ Physiol* 285: H2382–H2391.
134. Federspiel WJ, Popel AS (1986) A theoretical analysis of the effect of the particulate nature of blood on oxygen release in capillaries. *Microvasc Res* 32: 164–189.
135. Page TC, Light WR, Hellums JD (1998) Prediction of microcirculatory oxygen transport by erythrocyte/hemoglobin solution mixtures. *Microvasc Res* 56: 113–126.
136. Stathopoulos NA, Nair PK, Hellums JD (1987) Oxygen transport studies of normal and sickle red cell suspensions in artificial capillaries. *Microvasc Res* 34: 200–210.
137. Severns ML, Adams JM (1982) The relation between Krogh and compartmental transport models. *J Theor Biol* 97: 239–249.
138. Chen X, Buerk DG, Barbee KA, et al. (2007) A model of NO/O₂ transport in capillary-perfused tissue containing an arteriole and venule pair. *Ann Biomed Eng* 35: 517–529.
139. Ye GF, Moore TW, Buerk DG, et al. (1994) A compartmental model for oxygen-carbon dioxide coupled transport in the microcirculation. *Ann Biomed Eng* 22: 464–479.
140. Hayashi T, Watabe H, Kudomi N, et al. (2003) A theoretical model of oxygen delivery and metabolism for physiologic interpretation of quantitative cerebral blood flow and metabolic rate of oxygen. *J Cereb Blood Flow Metab* 23: 1314–1323.
141. Vadapalli A, Pittman RN, Popel AS (2000) Estimating oxygen transport resistance of the microvascular wall. *Am J Physiol Heart Circ Physiol* 279: H657–H671.
142. d'Angelo C (2007) Multiscale modelling of metabolism and transport phenomena in living tissues. Lausanne: PhD Thesis, EPFL.
143. Eggleton CD, Vadapalli A, Roy TK, et al. (2000) Calculations of intracapillary oxygen tension distributions in muscle. *Math Biosci* 167: 123–143.
144. Lucker A, Weber B, Jenny P (2015) A dynamic model of oxygen transport from capillaries to tissue with moving red blood cells. *Am J Physiol Heart Circ Physiol* 308: H206–H216.
145. Rees SE, Klastrup E, Handy J, et al. (2010) Mathematical modelling of the acid-base chemistry and oxygenation of blood: a mass balance, mass action approach including plasma and red blood cells. *Eur J Appl Physiol* 108: 483–494.
146. Dash RK, Bassingthwaighte JB (2004) Blood HbO₂ and HbCO₂ dissociation curves at varied O₂, CO₂, pH, 2,3-DPG and temperature levels. *Ann Biomed Eng* 32: 1676–1693.
147. Dash RK, Bassingthwaighte JB (2010) Erratum to: blood HbO₂ and HbCO₂ dissociation curves at varied O₂, CO₂, pH, 2,3-DPG and temperature levels. *Ann Biomed Eng* 38: 1683–1701.

148. Schacterle RS, Adams JM, Ribando RJ (1991) A theoretical model of gas transport between arterioles and tissue. *Microvasc Res* 41: 210–228.
149. Li Z, Yipintsoi T, Bassingthwaite JB (1997) Nonlinear model for capillary-tissue oxygen transport and metabolism. *Ann Biomed Eng* 25: 604–619.
150. Vadapalli A, Goldman D, Popel AS (2002) Calculations of oxygen transport by red blood cells and hemoglobin solutions in capillaries. *Artif Cells Blood Substit Immobil Biotechnol* 30: 157–188.
151. Cabrera ME, Saidel GM, Kalhan SC (1998) Role of O₂ in regulation of lactate dynamics during hypoxia: mathematical model and analysis. *Ann Biomed Eng* 26: 1–27.
152. Chen HS, Gross JF (1979) Estimation of tissue-to-plasma partition coefficients used in physiological pharmacokinetic models. *J Pharmacokinet Biopharm* 7: 117–125.
153. Sharan M, Popel AS (2002) A compartmental model for oxygen transport in brain microcirculation in the presence of blood substitutes. *J Theor Biol* 216: 479–500.
154. Hsu R, Secomb TW (1989) A Green's function method for analysis of oxygen delivery to tissue by microvascular networks. *Math Biosci* 96: 61–78.
155. Secomb TW, Hsu R, Park EY, et al. (2004) Green's function methods for analysis of oxygen delivery to tissue by microvascular networks. *Ann Biomed Eng* 32: 1519–1529.
156. Secomb TW (2016) A Green's function method for simulation of time-dependent solute transport and reaction in realistic microvascular geometries. *Math Med Biol* 33: 475–494.
157. Lamkin-Kennard KA, Buerk DG, Jaron D (2004) Interactions between NO and O₂ in the microcirculation: a mathematical analysis. *Microvasc Res* 68: 38–50.
158. Sriram K, Vazquez BY, Yalcin O, et al. (2011) The effect of small changes in hematocrit on nitric oxide transport in arterioles. *Antioxid Redox Signal* 14: 175–185.
159. Gundersen SI, Chen G, Palmer AF (2009) Mathematical model of NO and O₂ transport in an arteriole facilitated by hemoglobin based O₂ carriers. *Biophys Chem* 143: 1–17.
160. Vullo V (2014) *Circular Cylinders and Pressure Vessels*. Springer.
161. Gonzalez-Fernandez JM, Ermentrout B (1994) On the origin and dynamics of the vasomotion of small arteries. *Math Biosci* 119: 127–167.
162. Achakri H, Rachev A, Stergiopoulos N, et al. (1994) A theoretical investigation of low frequency diameter oscillations of muscular arteries. *Ann Biomed Eng* 22: 253–263.
163. Carlson BE, Arciero JC, Secomb TW (2008) Theoretical model of blood flow autoregulation: roles of myogenic, shear-dependent, and metabolic responses. *Am J Physiol Heart Circ Physiol* 295: H1572–H1579.
164. Ford Versypt AN, Makrides E, Arciero JC, et al. (2015) Bifurcation study of blood flow control in the kidney. *Math Biosci* 263: 169–179.
165. Carlson BE, Secomb TW (2005) A theoretical model for the myogenic response based on the length-tension characteristics of vascular smooth muscle. *Microcirculation* 12: 327–338.
166. Arciero J, Harris A, Siesky B, et al. (2013) Theoretical analysis of vascular regulatory mechanisms contributing to retinal blood flow autoregulation. *Invest Ophthalmol Vis Sci* 54: 5584–5593.
167. Ursino M, Di Giammarco P (1991) A mathematical model of the relationship between cerebral blood volume and intracranial pressure changes: the generation of plateau waves. *Ann Biomed Eng* 19: 15–42.
168. Ursino M (1988) A mathematical study of human intracranial hydrodynamics part 1—The

- cerebrospinal fluid pulse pressure. *Ann Biomed Eng* 16: 379–401.
169. Banaji M, Tachtsidis I, Delpy D, et al. (2005) A physiological model of cerebral blood flow control. *Math Biosci* 194: 125–173.
 170. Beard DA, Bassingthwaite JB (2001) Modeling advection and diffusion of oxygen in complex vascular networks. *Ann Biomed Eng* 29: 298–310.
 171. Jespersen SN, Ostergaard L (2012) The roles of cerebral blood flow, capillary transit time heterogeneity, and oxygen tension in brain oxygenation and metabolism. *J Cereb Blood Flow Metab* 32: 264–277.
 172. Lemon DD, Nair PK, Boland EJ, et al. (1987) Physiological factors affecting O₂ transport by hemoglobin in an in vitro capillary system. *J Appl Physiol* 62: 798–806.
 173. Goldman D, Popel AS (2000) A computational study of the effect of capillary network anastomoses and tortuosity on oxygen transport. *J Theor Biol* 206: 181–194.
 174. Tsoukias NM, Popel AS (2003) A model of nitric oxide capillary exchange. *Microcirculation* 10: 479–495.
 175. Delp MD, Armstrong RB (1988) Blood flow in normal and denervated muscle during exercise in conscious rats. *Am J Physiol* 255: H1509–H1515.
 176. Pohl U, De Wit C, Gloe T (2000) Large arterioles in the control of blood flow: role of endothelium-dependent dilation. *Acta Physiol Scand* 168: 505–510.
 177. Segal SS (2005) Regulation of blood flow in the microcirculation. *Microcirculation* 12: 33–45.
 178. Harris A, Jones-Cuypers CP, Kagemann L, et al. (2003) Atlas of ocular blood flow: vascular anatomy, pathophysiology, and metabolism. Butterworth-Heinemann/Elsevier.
 179. Aletti M, Gerbeau JF, Lombardi D (2016) A simplified fluid-structure model for arterial flow. Application to retinal hemodynamics. *Comput Methods Appl Mech Engrg* 306: 77–94.
 180. Causin P, Malgaroli F (2016) Mathematical modeling of local perfusion in large distensible microvascular networks. arXiv:161002292 [q-bio.TO].
 181. Carichino L, Guidoboni G, Siesky B, et al. (2013) Effect of intraocular pressure and cerebrospinal fluid pressure on the blood flow in the central retinal vessels, In: Causin P, Guidoboni G, Sacco R et al., Editors, *Integrated Multidisciplinary Approaches in the Study and Care of the Human Eye*, Kugler Publications, 59–66.
 182. Cassani S, Arciero J, Guidoboni G, et al. (2016) Theoretical predictions of metabolic flow regulation in the retina. *J Model Ophthalmol* 1.
 183. Yu DY, Cringle SJ (2001) Oxygen distribution and consumption within the retina in vascularised and avascular retinas and in animal models of retinal disease. *Prog Retin Eye Res* 20: 175–208.
 184. Yu DY, Cringle SJ, Su EN (2005) Intraretinal oxygen distribution in the monkey retina and the response to systemic hyperoxia. *Invest Ophthalmol Vis Sci* 46: 4728–4733.
 185. Roos MW (2004) Theoretical estimation of retinal oxygenation during retinal artery occlusion. *Physiol Meas* 25: 1523–1532.
 186. Haugh LM, Linsenmeier RA, Goldstick TK (1990) Mathematical models of the spatial distribution of retinal oxygen tension and consumption, including changes upon illumination. *Ann Biomed Eng* 18: 19–36.
 187. Cornelissen AJ, Dankelman J, VanBavel E, et al. (2002) Balance between myogenic, flow-dependent, and metabolic flow control in coronary arterial tree: a model study. *Am J Physiol Heart Circ Physiol* 282: H2224–H2237.

188. He Z, Lim JK, Nguyen CT, et al. (2013) Coupling blood flow and neural function in the retina: a model for homeostatic responses to ocular perfusion pressure challenge. *Physiol Rep* 1: e00055.
189. Ursino M (1991) Mechanisms of cerebral blood flow regulation. *Crit Rev Biomed Eng* 18: 255–288.
190. Ursino M (1991) A mathematical model of overall cerebral blood flow regulation in the rat. *IEEE Trans Biomed Eng* 38: 795–807.
191. Nobrega AC, O’Leary D, Silva BM, et al. (2014) Neural regulation of cardiovascular response to exercise: role of central command and peripheral afferents. *Biomed Res Int* 2014: 478965.
192. Sigal IA, Ethier CR (2009) Biomechanics of the optic nerve head. *Exp Eye Res* 88: 799–807.
193. Downs JC, Roberts MD, Burgoyne CF, et al. (2009) Multiscale finite element modeling of the lamina cribrosa microarchitecture in the eye. *Conf Proc IEEE Eng Med Biol Soc* 2009: 4277–4280.
194. Grytz R, Girkin CA, Libertiaux V, et al. (2012) Perspectives on biomechanical growth and remodeling mechanisms in glaucoma. *Mech Res Commun* 42: 92–106.
195. Newson T, El-Sheikh A (2006) Mathematical modeling of the biomechanics of the lamina cribrosa under elevated intraocular pressures. *J Biomech Eng* 128: 496–504.
196. Harris A, Guidoboni G, Arciero JC, et al. (2013) Ocular hemodynamics and glaucoma: the role of mathematical modeling. *Eur J Ophthalmol* 23: 139–146.
197. Guidoboni G, Harris A, Carichino L, et al. (2014) Effect of intraocular pressure on the hemodynamics of the central retinal artery: a mathematical model. *Math Biosci Eng* 11: 523–546.
198. Cassani S, Harris A, Siesky B, et al. (2015) Theoretical analysis of the relationship between changes in retinal blood flow and ocular perfusion pressure. *J Coupled Syst Multiscale Dyn* 3: 38–46.
199. Causin P, Guidoboni G, Harris A, et al. (2014) A poroelastic model for the perfusion of the lamina cribrosa in the optic nerve head. *Math Biosci* 257: 33–41.
200. Biesecker KR, Srien AI, Shimoda AM, et al. (2016) Glial cell Calcium signaling mediates capillary regulation of blood flow in the retina. *J Neurosci* 36: 9435–9445.



AIMS Press

© 2017 Paola Causin, et al., licensee AIMS Press. This is an open access article distributed under the terms of the Creative Commons Attribution License (<http://creativecommons.org/licenses/by/4.0>)